UNIVERSITY OF CALIFORNIA

MERCED

Core/Shell Heterojunction Nanowire Solar Cell Fabricated by Lithographically Patterned Nanowire Electrodeposition Method

DISSERTATION

submitted in partial satisfaction of the requirements for the degree of

DOCTOR OF PHILOSOPHY

in Physics

by

Somnath Ghosh

Dissertation Comittee:

Professor Erik J. Menke, Adviser

Professor Jay E. Sharping, Chair

Professor Michael Scheibner

Professor M. Saif Islam

2012

The dissertation of Somnath Ghosh is approved, and is acceptable in quality and form for publication on microfilm:

Committee on Graduate Work

_____

Adviser Professor Erik J. Menke

_____

Chair Professor Jay E. Sharping

_____

Professor Michael Scheibner

_____

Professor M. Saif Islam

University of California, Merced

2012

Dedicated To

two amazing girls in my life,

my loving wife Meenakshi and my cute little daughter

Aanya

Contents

List of Figures

List of Tables

Acknowledgement

I would like to express my deepest respect and gratitude to everyone who have supported me over the years to achieve my dreams. First and foremost, I would like to thank my advisor, Prof. Erik Menke. Erik who has been both an incredible advisor and an inspiration to me. Erik taught me how to deal tough situations by being calm and cool. I would like to thank my sweet wife, Meenakshi for holding my hands and walking with me at each and every steps of my life. She is the best thing ever happened to me. Without her, I don't see myself closer to what I am today. There are few other people I would like to thank. First is my parents for motivating me to pursue my dreams. Then my late grandpa Dr. Umapada Ghosh for being an inspiration. I would like to thank all my close friends especially Yashwant Verma for being there always to help me in every possible way. I would like to thank all my colleagues at UC Merced especially Justin Hujdic, Luke Reed and Alan Sargisian for all the help and support during my stay in the lab. I would really like to thank all my Professors at UC Merced. Prof. Jay Sharping for being the chair of my PhD committee and guiding me through all the procedures to achieve my goal. Prof. Michael Scheibner for being the member of my PhD committee and for the helpful discussion throughout my grad study. Prof. M. Saif Islam for being the external member of the committee and driving all the way from Sacramento for my PhD defense. Prof. Raymond Chiao for teaching me one of the best Quantum mechanics course I ever studied so far. I would like to thank ICEM at UC Davis and TEM lab at UC Berkeley for letting us use all the instruments. I would really like to

thank Michael Brenner and Dr. Nerissa Draeger for giving me a chance to work as an intern in Low-k flowable oxide team at Novellus Systems, San Jose. I would finally like to acknowledge the funding sources that provided monetary support for my research. Specifically the startup funds from UC Merced, UCMERI and graduate research council for funding part of my summer fellowships.

Curriculum Vitae

Somnath Ghosh

2002	B.Sc. in Physics with Honors University of Calcutta, India
2004	M.Sc. in Physics, School of Pure and Applied Physics G. G. University (Central University), India
2004-2005	Junior Research Fellow, IC Design and Fabrication Center, Jadavpur University, India
2005-2006	Process Development Engineer, KPE Solar Co Ltd., South Korea
2006-2007	Senior Research Fellow, Microelectronics Group and AMAT, IIT Bombay, India
2007-2012	Teaching Fellow, Department of Physics University of California, Merced
2011	Process Development Engineer Intern, Gapfill BU/DGS Novellus Systems, San Jose
2012	PhD in Physics University of California, Merced Dissertation: Core/Shell Heterojunction Nanowires Fabricated by LPNE method: Photodiode and Photovoltaic Characteristics. Professor Erik J. Menke, Adviser

Publications

S. N. Ghosh, J. E. Hujdic and E. J. Menke. Au/CIS/CdS Coaxial Heterojunction Nanowire Solar Cell fabricated by LPNE method, *in preparation.*

Somnath Ghosh, Justin Hujdic and Erik Menke. Gold Core–Semiconductor Shell Nanowires Prepared by Lithographically Patterned Nanowire Electrodeposition, *Journal of Physical Chemistry C,*115:17670, 2011.

S. N. Ghosh, B. B. Buckley, C. G. L. Ferri, X. Li, F. M. Mendoza, Y. K. Verma, N. Samarth, D. D. Awschalom, and S. Ghosh. Polarization based control of optical hysteresis in coupled GaAs microdisks, *Appl. Phys. Lett.* 97:011106, 2010.

Chi-Cheng Fu, Anthony Grimes, Maureen Long, Christopher G.L. Ferri, Brent D. Rich, Somnath Ghosh, Ajay Gopinathan, Sayantani Ghosh, Luke P. Lee, *and* Michelle Khine. Tunable Nanowrinkles on Shape Memory Polymers Sheets, *Advanced Materials,*21:1, 2009.

Y. K. Verma, R. H. Inman, C. G. L. Ferri, H. Mirafzal, S. N. Ghosh, D. F. Kelley, L. S. Hirst, W. C. Chin, and S. Ghosh. Electrical modulation of static and dynamic spectroscopic properties of coupled nanoscale GaSe quantum dot assemblies. *Phys. Rev. B* 82:165428, 2010.

S. N. Ghosh, I. O.Parm, K.S. Jang, S. K. Dhungel, S.W. Jung and J. Yi. Field Induced Passivation of P- Type Silicon by Using AlON Films, *Renewable Energy*, 33:320, 2008.

Eung Kwon Kim, Tae Yong Lee, Yong Seob Park, Somnath Ghosh, Byungyou Hong, Young Sung Kim and Joon Tae Song. Improved crystallization characteristics of ZnO thin film grown onto a-C:H film used as a buffer layer, *Thin Solid Films* , 515:4988, 2007

S. K. Dhungel, J.Yoo, K.Kim, S.N.Ghosh, S.W.Jung and J.Yi. Process Induced Variation in the Measurement of Minority Carrier Life Time of Silicon in Solar Cells Fabrication, *Material Science and Engineering B* 134:287, 2006

S.K.Dhungel, J.Yoo, S.Jung, S.N.Ghosh, J. Yi. Study of Electrical Properties of Oxidized Porous Silicon for Back Surface Passivation of Silicon Solar Cell, *Renewable Energy*, 33:282, 2008.

S.N.Ghosh, I.O.Parm, K.S.Jang, S.K.Dhungel, S.Jung, J.Yi. Effect of Rapid Thermal Oxidation on Fixed Negative Charge of Sputtered Film of Aluminium Nitride, *under review to Thin Solid Films.*

S.N.Ghosh, D.Bora, S.K.Dhungel, J.Yoo, M.Gowtham, J.Yi. Study of High Density Helicon Plasma generation and measurement of plasma parameters using frequency compensated Langmuir probe, *Journal of Korean Physical Society,*48:908, 2006

S.K.Dhungel, J.Yoo, S.Jung, S.N.Ghosh, J.Yi. Double Layer Antireflection Coating of MgF2/SiNX for Crystalline Silicon Solar Cell, *Journal of Korean Physical Society*, 49:885, 2006.

Abstract of the Dissertation

Core/Shell Heterojunction NWs Fabricated by LPNE method:

Photodiode and Photovoltaic Characteristics

by
Somnath Ghosh

Doctor of Philosophy in Physics

University of California, Merced, 2012

Professor Erik J. Menke, Adviser

Lithographically Patterned NW Electrodeposition (LPNE) is a new technique for preparing NWs that was developed by Prof. Erik Menke while he was doing his research in Penner group in 2006. Here, we discuss some of the common problems in state of the art solar cell technology and how we can effectively use LPNE to make next generation Core/Shell NW based solar cells and NIR photodetectors. The first step in the process is the synthesis of Au/PbSe and Au/copper indium diselenide (CIS) core/shell NWs using LPNE. The NWs were synthesized by the aqueous electrodeposition of either PbSe or CIS onto gold NWs prepared by LPNE. The resulting NWs are nanocrystalline, exhibit a sharp boundary between the gold core and the semiconducting coating, and are photoconductive, with enhanced light absorption in smaller NWs which could be due to the cavity effect of the semiconductor shell NWs. The second step is the synthesis of Au/CIS/CdS core/shell/shell based p-n heterojunction NW based solar cells by electrodepositing CdS on top of Au/CIS core/shell NWs. Core/Shell NW based devices prepared by above method

are cheap and can be fabricated on cheap substrates like plastics or glass. This technique also gives us the control over size, shape and orientation of the NWs. The beauty of this method is that it gives us a platform to understand some of the basic device physics problems by characterizing each single NW electrically or optically.

Chapter 1

Nanomaterials for Next Generation Photovoltaics

1.1 Objectives of the Dissertation

The dissertation has four main parts. The first of these is this introduction, where I give a brief overview on the common problems like light trapping and minority carrier diffusion length of the first and second generation solar cell technology and current experiments being performed by different groups on plasmonics and semiconductor cavities to improve the solar cell efficiency. I have also discussed how core/shell structure could improve the solar cell efficiency. The second part is an in depth experimental study to understand the light matter interaction in semiconductor cavities and surface plasmons. This part of my work helped me to find the answers regarding light matter interaction in nanoscale system which intern helped me to make efficient nanowires based devices. The third part describes how I addressed the shortcoming of the present solar cell technology by synthesizing metal/semiconductor core/shell heterostructure NWs using LPNE method. In this part I have also discussed about the Optoelectronic measurements of the devices based on these coaxial NWs showing enhanced absorption efficiency of incident light. Finally, in the fourth part I have described the fabrication of core/shell p-n heterojunction NW solar cells and detailed study of the device parameters by tuning the semiconductor shell widths.

1.2 Photovoltaics or Solar Cells

The conversion of photons to electricity is commonly known as photovoltaics and it is one of the well researched technology that may help to generate electrical power. Worldwide photovoltaic

production was more than 5 GW in 2008, and is expected to rise above 20 GW by 2015. Generating the power from solar cells is an expensive process and to commercialize this process, the cost needs to be of the order or less than resources available in nature. Since the invention of solar cells, the solar market is mainly dominated by crystalline silicon (c-Si) solar cells [1] because of high power throughput. The problem with this technology is that the wafers used for solar cell fabrication are very thick ranging between 150-300 μm and this itself increases the cost of production. To overcome this problem scientists started studying the second generation of solar cell which is mainly based on thin film technology. Thin film solar cells use an average thickness of 1-2 μm absorber material which is 100 times thinner than the c-Si. Thin film solar cell can be deposited on cheap module-sized substrates such as glass, plastic or stainless steel. Thin-film solar cells are made from a variety of semiconductors including amorphous and polycrystalline Si, GaAs, CdTe and $CuInSe_2$, as well as organic semiconductors. The common problem in all thin-film solar-cell technologies is that the absorbance of near-bandgap light is small, in particular for the indirect-bandgap semiconductor Si. Therefore, structuring the thin-film solar cell so that light is trapped inside to increase the absorbance is very important.

Light trapping or Photon management in c-Si solar cell is achieved by pyramidal surface texurization as shown in Fig. 1.1. Any "roughening" of the surface reduces reflection by increasing the chances of reflected light bouncing back onto the surface, rather than out to the surrounding air.

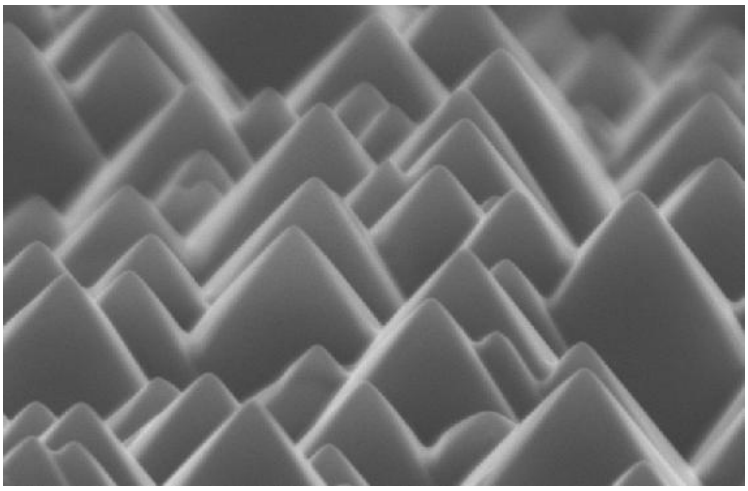

Figure.1.1 Scanning electron microscope photograph of a textured Silicon surface [1]

Such kind of structures are not possible in second generation solar cells because it will defeat the purpose of having thin films for solar cells.

A new method of light trapping in second generation or third generation (nanostructured or dye sensitized based) solar cells is by using of metallic nanostructures that support surface plasmons [2]. Plasmons are the excitations of the conduction electrons at the interface between a metal and a dielectric. By choosing the proper geometry of these metal nanostructures, light can be concentrated by several folds of the wavelength thereby increasing the absorption. Surface plasmons could be localized like the one excited in metal nanoparticles or they could be mobile like cloud which are called surface plasmon polaritons (SPPs) propagating at the metal/semiconductor interface are of interest. Plasmonics: Plasmon based electronics has been studied rigorously for past few years. It has opened a new channel to do the basic experiments on nanophotonics and quantum teleportation. There are several research paper showing the study of the coupling of plasmons to optical emitters[3-5]; plasmon focusing[6,7];hybridized plasmonic modes in nanoscale metal shells[8]; nanoscale wave guiding[9-12]; nanoscale optical

antennas[13]; plasmonic integrated circuits[14,15]; nano scale switches[16]; plasmonic lasers[17-19]; surface-plasmon-enhanced light-emitting diodes[20]; imaging below the diffraction limit[21]; and materials with negative refractive index[22-24].

In addition to plasmonics, more advanced light trapping techniques based on resonant cavities[25], have recently gained a lot of attention. When the incident wavelength is in resonance with these structures, several folds of wavelength gets trapped in the form of resonant modes. The best possible light trapping technology would effectively trap light in a broad-band, angle independent, and polarization-independent manner. Resonant cavity structures are potential candidates, but their performance is typically limited by light absorption and emission at different wavelength range. Resonant structures tend to absorb and emit light in a particular angle which is a drawback for making devices based on these kind of structures. Arrays of semiconductor nanostructures with elongated shapes, such as NWs (NWs), nanorods, and nanopillars, have recently demonstrated significant promise for photovoltaic applications; these structures can exhibit both enhanced absorption and a reduced reflectivity as compared to planar, film-based devices.

1.3 Plasmonics for Light harvesting

Absorber material in a conventional Solar cell must be thick enough to allow complete light absorption and photo generated current collection. Plasmonic structures can offer at least three ways of reducing the physical thickness of the photovoltaic absorber layers while keeping their optical thickness constant as discussed by Atwater et al. [26]. First, metallic nanoparticles can be used as subwavelength scattering elements to couple and trap freely propagating plane waves from the Sun into an absorbing semiconductor thin film, by folding the light into a thin absorber

layer (Fig. 1.2a). Second, metallic nanoparticles can be used as subwavelength antennas in which the plasmonic near-field is coupled to the semiconductor, increasing its effective absorption cross-section (Fig. 1.2b). Third, a corrugated metallic film on the back surface of a thin photovoltaic absorber layer can couple sunlight into SPP modes supported at the metal/semiconductor interface as well as guided modes in the semiconductor slab, whereupon the light is converted to photocarriers in the semiconductor (Fig. 1.2c).

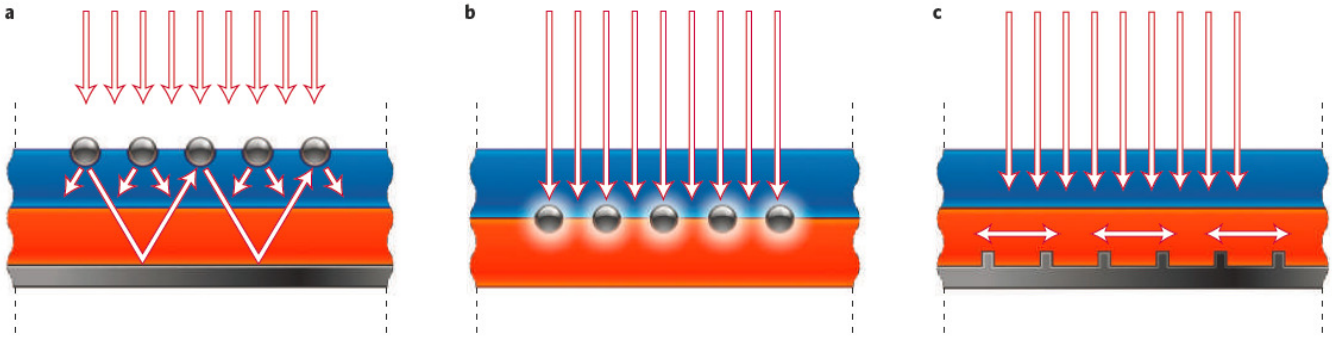

Figure 1.2 Plasmonic light-trapping geometries for thin-film solar cells. a, Light trapping by scattering from metal nanoparticles at the surface of the solar cell. Light is preferentially scattered and trapped into the semiconductor thin film by multiple and high-angle scattering, causing an increase in the effective optical path length in the cell. b, Light trapping by the excitation of localized surface plasmons in metal nanoparticles embedded in the semiconductor. The excited particles' near-field causes the creation of electron–hole pairs in the semiconductor. c, Light trapping by the excitation of surface plasmon polaritons at the metal/semiconductor interface. A corrugated metal back surface couples light to surface plasmon polariton or photonic modes that propagate in the plane of the semiconductor layer [26].

The enhanced coupling of light into semiconductor thin films by scattering from plasmonic nanoparticles was first discovered by Stuart and Hall. They used dense nanoparticle arrays as resonant scattering centers to couple light into Si-on-insulator photo detector structures [27,28]. They recorded a roughly 20-fold increase in the infrared photocurrent in such a structure. This research field then remained relatively untouched for many years, until applications in thin-film

solar cells emerged, with papers published on enhanced light coupling into single-crystalline Si [29], amorphous Si [30,31], Si-on-insulator [32], quantum well [33] and GaAs [34] solar cells covered with metal nanoparticles.

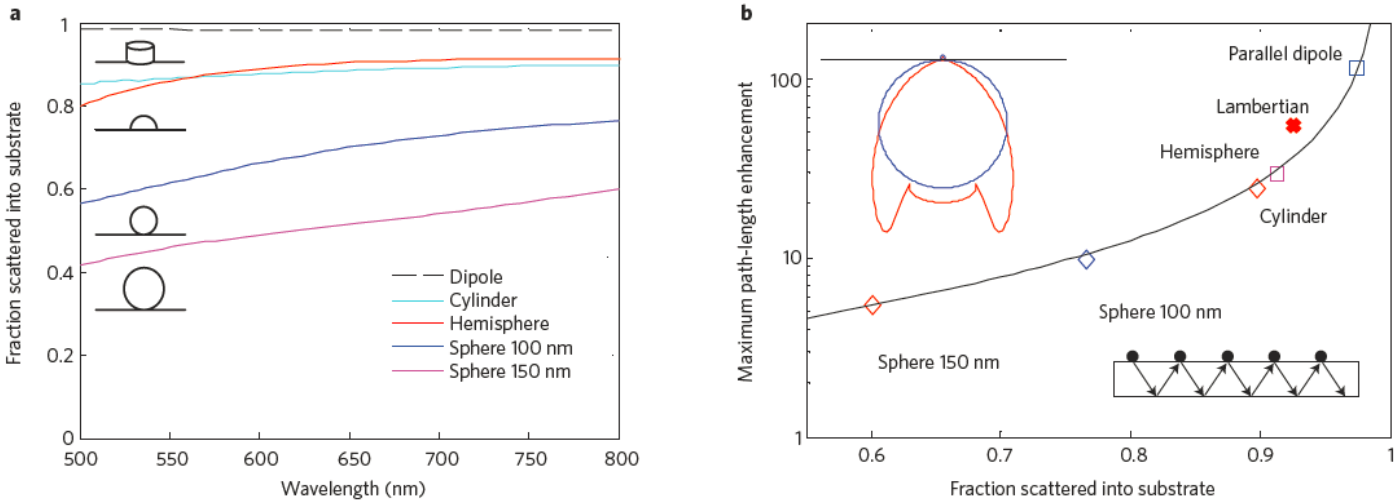

Figure 1.3 Light scattering and trapping is very sensitive to particle shape**.** (a) Fraction of light scattered into the substrate, divided by total scattered power, for different sizes and shapes of Ag particles on Si. Also plotted is the scattered fraction for a parallel electric dipole that is 10 nm from a Si substrate. (b), Maximum path-length enhancement, according to a first-order geometrical model, for the same geometries as in **a** at a wavelength of 800 nm. Absorption within the particles is neglected for these calculations, and an ideal rear reflector is assumed. The line is a guide for the eye. Insets: (top left) angular distribution of scattered power for a parallel electric dipole that is 10 nm above a Si surface (red) and a Lambertian scatterer (blue); (lower right) geometry considered for calculating the path-length enhancement [26]

In recent papers [35,36], Polman's group has reported that the shape and size of metal nano particles are key factors determining the coupling efficiency. This is shown in Fig. 1.3a, which shows that smaller particles, with their effective dipole moment located closer to the semiconductor layer, couple a larger amount of the incident light into the under lying semiconductor because of enhanced near-field coupling. Infact, in the limit of a point dipole very near to a silicon substrate, 96% of the incident light is scattered into the substrate, demonstrating

the power of the particle scattering technique. Figure 1.3b shows the increment of the path-length in the solar cell derived from Fig. 1.3a using a simple first-order scattering model. For 100-nm-diameter Ag hemispheres on Si, a 30-fold enhancement is found. These light-trapping effects are most pronounced at the peak of the Plasmon resonance spectrum, which can be tuned by engineering the dielectric constant of the surrounding matrix. For example, small Ag or Au particles in air have Plasmon resonances at 350 nm and 480 nm respectively; they can be red-shifted in a controlled way over the entire 500–1500 nm spectral range by (partially) embedding them in SiO_2, Si_3N_4 or Si [37-39].

1.4 Resonant Cavities for Light Trapping in Solar Cell

Understanding the optical response of NW's to the solar radiation is still rapidly growing area of research, and a deep fundamental knowledge of their optical properties is key to the design of future generations of high performance NW solar cells. The NWs capture and absorb significantly more solar photons than an equivalent volume of bulk material. Recently, powerful antenna effects were experimentally demonstrated in photocurrent measurements on Ge NWs [40] at specific wavelengths. When the illumination wavelength matched one of the allowed leaky mode resonances (LMRs), the high refractive index wire is able to capture and trap the light by multiple internal reflections from its boundary as shown in Fig. 1.4. As a result, light absorption and the resulting photocurrent could be enhanced at a desired wavelength by tuning the NW diameter. LMR was originally developed for micrometer-scale resonators. LMR in optical fibers and micro scale dielectric resonators is based on classical waveguide theory.

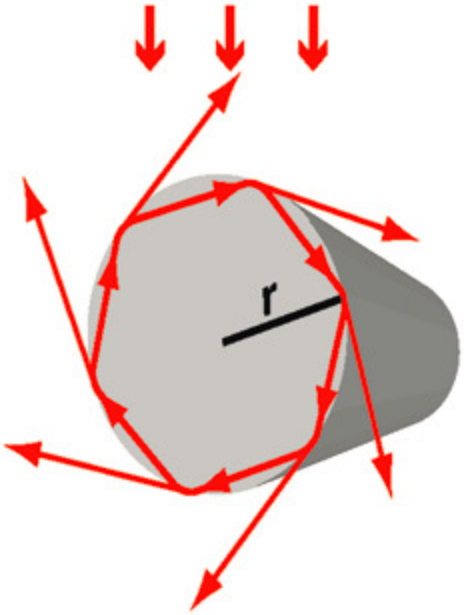

Figure 1.4. Schematics showing the generation of leaky mode resonance in semiconductor NWs [40]

By solving Maxwell's equations with the appropriate boundary conditions, it follows that excitation of leaky modes occurs in an infinitely long dielectric cylinder of radius a when the following condition is satisfied:

$$\left(\frac{1}{\kappa^2}-\frac{1}{\gamma^2}\right)^2\left(\frac{\beta m}{a}\right)^2=\kappa_0^{\,2}\left(n^2\frac{J_m'(\kappa a)}{J_m(\kappa a)}-n_0^{\,2}\frac{H_m'(\gamma a)}{\gamma H_m(\gamma a)}\right)\left(\frac{J_m'(\kappa a)}{\kappa J_m(\kappa a)}-\frac{H_m'(\gamma a)}{\gamma H_m(\gamma a)}\right) \qquad (1)$$

where $\gamma(\kappa)$ and $n_0(n)$ are the transverse wave vector and refractive index outside (inside) the cylinder, β and κ_0 are the wave vectors along the cylindrical axis and in free space, J_m and H_m are the mth-order Bessel function of the first kind and Hankel function of the first kind and the prime denotes differentiation with respect to related arguments. For normal-incidence illumination (β = 0) of a cylinder in vacuum (n_0= 1), equation (1) can be split into conditions for purely transverse-magnetic modes with the magnetic fields in the plane normal to the NW axis $\left[nJ_m'(n\kappa_0 a)/J_m(n\kappa_0 a)=H_m'(\kappa_0 a)/H_m(\kappa_0 a)\right]$ and transverse electric modes

$\left[J_m'(n\kappa_0 a)/nJ_m(n\kappa_0 a) = H_m'(\kappa_0 a)/H_m(\kappa_0 a) \right]$ with the electric fields normal to the NW axis. From these conditions, it follows that NWs tend to support a limited number of transverse-electric and transverse-magnetic LMRs, which increase in number as their radius is increased.

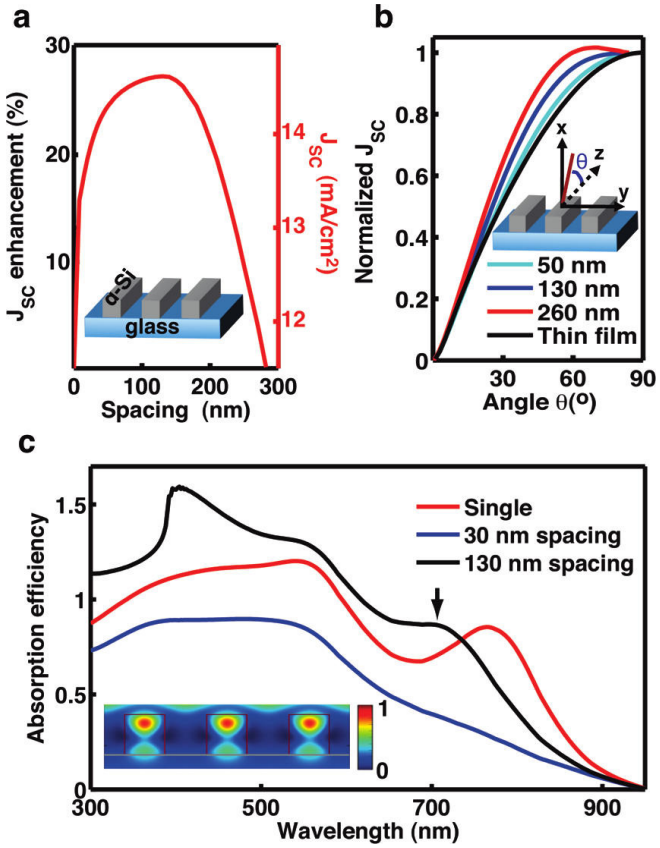

Figure 1.5. Photocurrent enhancement and optical resonances in rectangular NW arrays on glass. (a) Calculated photocurrent density *J*sc of an array of 130 nm wide square NWs as a function of the NW separation. The left-side vertical axis indicates the photocurrent normalized to that of a continuous film (zero separation). Inset, schematic illustration of the array structure. (b) Calculated dependence of the photocurrent density *J*sc on the illumination angle for the array with various spacings (50, 130 and 260 nm) and a 130 nm thick film. The incident angle is changed in the *xz* plane, while the NWs are aligned along the *z* axis. (c) Calculated absorption spectra of a 130 nm wide square NW in the array with different separations of 30 and 130 nm. The red line is the absorption spectra of a single NW on the same substrate. The broad absorption spectrum of the array with the 130 nm spacing strongly resembles that of a single NW [41].

Mark Brongersma's group at Stanford has shown that the use of LMR-induced field enhancements inside nanostructures [41] to spectrally tune and enhance fundamental absorption properties. This work shows that light absorption in NW devices is not just a function of the intrinsic optical materials properties, but also can be engineered through control over the size, geometry and orientation of the nanostructure as shown in Fig. 1.5. This work has also shown the calculated values of *J*sc for normal-incidence illumination and corresponding enhancement for cylindrical NWs made from popular semiconductors in solar applications, including germanium (Ge), amorphous silicon (R-Si), CdTe, CuInGaSe, and gallium arsenide (GaAs). All materials systems show significant enhancements and similar trends in the dependence on the NW size. For all of the semiconductors, *J*sc tends to show good enhancements and little angle dependence when the NW size is optimized to again match the second peak in the plots of photocurrent vs size as shown in Fig 1.6.

The concept of using LMRs of semiconductor structures is extremely general and can be applied to engineer absorption spectra for a wide variety of semiconductor materials and object geometries. Key applications that can directly benefit from the observed absorption enhancements are NW-based solar cells and photodetectors.

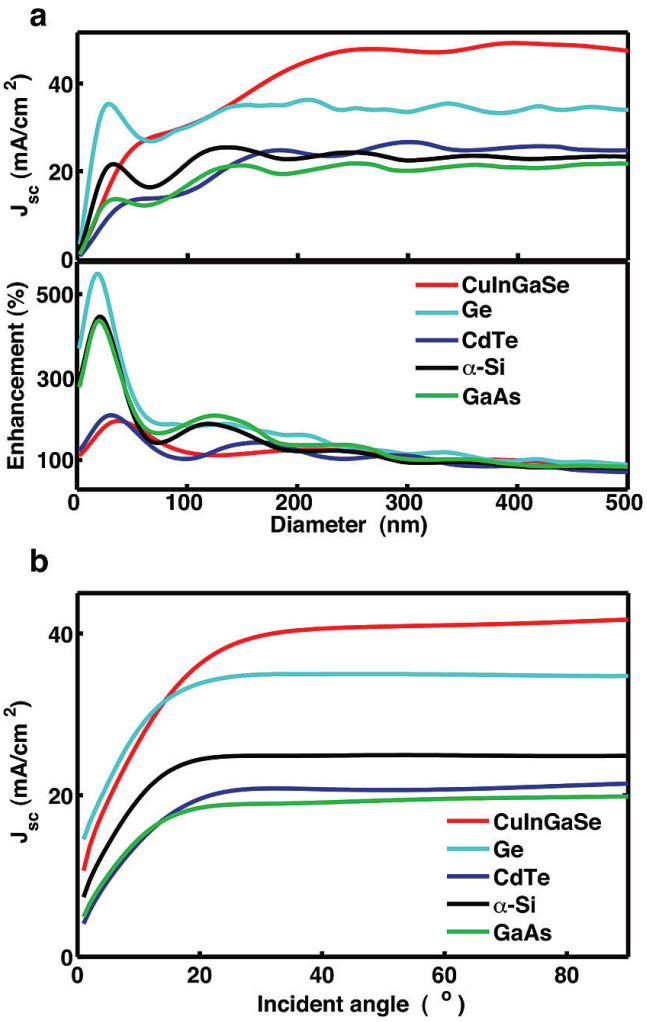

Figure 1.6. Generality of the photocurrent enhancement and minimized angle dependence of the photocurrent from individual semiconductor NWs: (a) (upper) short circuit photocurrent density *J*sc in NWs of other major photovoltaic materials, including CuInGaSe, Ge, CdTe, amorpous Si, and GaAs, and (lower) photocurrent enhancement in the NWs compared to their bulk counterparts. (b) Minimized dependence of *J*sc of various semiconductor NWs on the incident angle. The diameters of the NWs are CuInGaSe, 180 nm, Ge, 140 nm, R-Si, 120 nm, CdTe, 140 nm, and GaAs, 120 nm, respectively. Those diameters match the excitation of the second-order LMRs [41].

1.5 How Core/Shell NWs can improve the efficiency

Making solar cells using materials besides Si may help reduce the cost but the efficiency of the cell will be less because of high defect levels and low minority carrier diffusion length.

According to an study performed by Nate Lewis and Hary Atwater from Caltech the use of such low diffusion-length materials as the absorbing base in a conventional planar *p-n* junction solar-cell geometry results in devices having a carrier collection limited by minority-carrier diffusion in the base region as shown in Fig. 1.7.

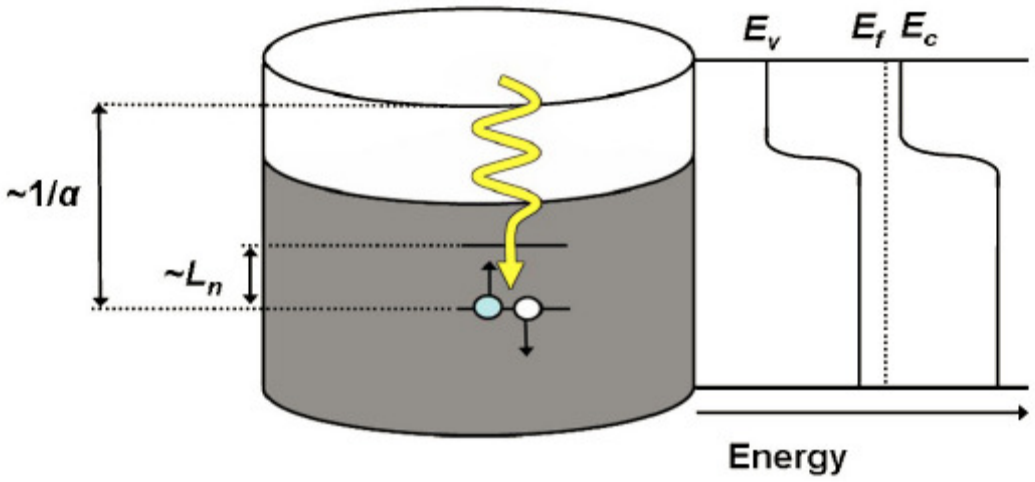

Figure 1.7. A conventional planar solar cell is a *p-n* junction device. Light penetration into the cell is characterized by the optical thickness of the material (1/α), noting that the absorption coefficient α is wavelength dependent while the mean-free path of generated minority carriers is given by their diffusion length. In the case shown, light penetrates deep into the cell, but the electron-diffusion length is too short to allow for the collection of all light-generated carriers [42].

Increasing the thickness of the base in such a cell will therefore produce more light absorption but will not result in an increase in device efficiency. In the absence of sophisticated light-trapping schemes, materials with low diffusion lengths and low absorption coefficients therefore cannot be readily incorporated into planar solar-cell structures with high energy-conversion efficiency [43].

The same group also proposed that an electronic device consisting of arrays of radial *p-n* junction nanorods (Fig. 1.8)may provide a solution to this device design and optimization issue.

A nanorod with a *p-n* junction in the radial direction would enable a decoupling of the requirements for light absorption and carrier extraction into orthogonal spatial directions. Each individual *p-n* junction nanorod in the cell could be long in the direction of incident light, allowing for optimal light absorption, but thin in another dimension, thereby allowing for effective carrier collection.

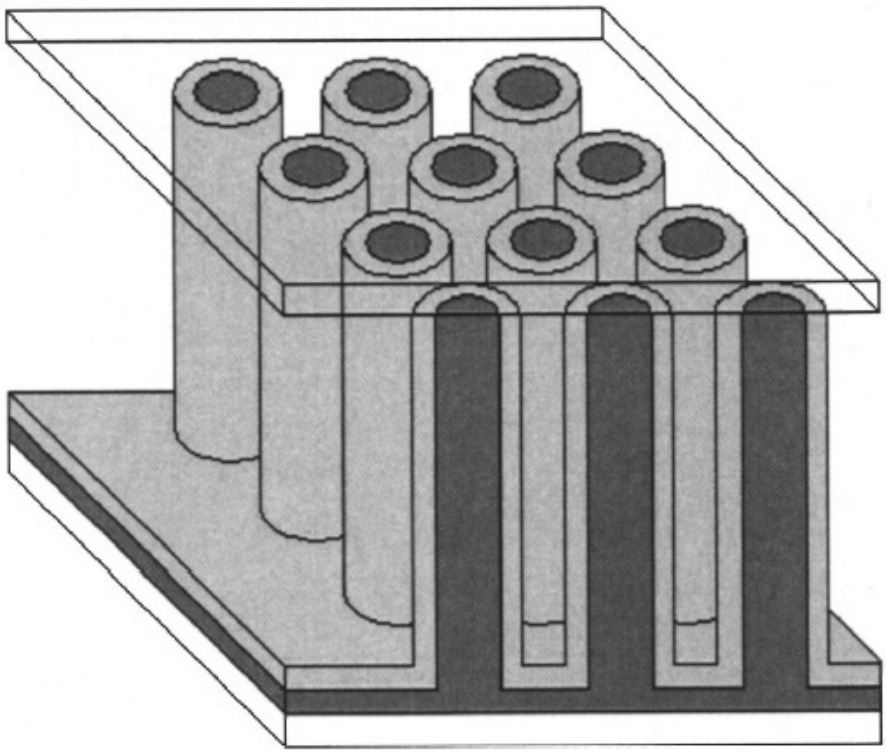

Figure 1.8. Schematic cross-section of the radial *p-n* junction nanorod cell. Light is incident on the top surface. The light grey area is *n* type, the dark grey area *p* type [42].

Chapter 2

Quantum Dots in Optical Microcavities and on roughened Metallic surface

2.1 Optical Bistability in coupled GaAs microdisks

2.1.1 Motivation

The optical microcavities, as shown in Fig. 2.1, are optical resonators of dimensions close to, or less than, the dimension of the wavelength of light and formed by reflecting faces on the sides of an optical medium.

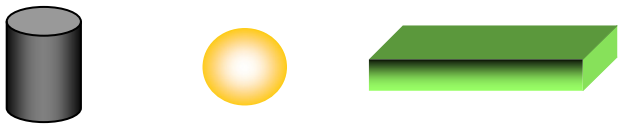

Figure 2.1 Possible geometries of Optical Microcavity

Microcavities could be of any material ranging from metals and dielectrics to semiconductors. Optical and electrical properties of semiconductors can be controlled and fine-tuned by growing binary-, tertiary-, or quaternary-alloys, thin-film hetero-junctions with mono-layer control on thickness, and nano-structures with controlled dimensions, thereby making them favorable choice as the active regions of microcavities. The selection of semiconducting materials is

primarily driven by the ability to prepare materials with the desired optical properties like photoluminescence.

Length scales of the microcavities are of two kinds, micron and submicron sized and they both use two different ways of confining the light.

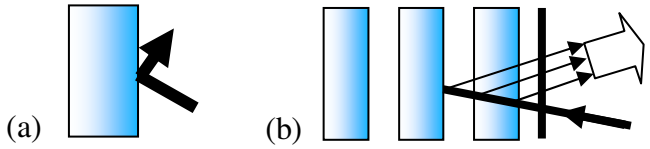

Figure 2.2 (a) Single interface reflection (Micrometer sized) and (b) interference from multiple interfaces (Sub micrometer sized)

A micron sized resonator as shown in fig. 2.2(a). It uses reflection from a single interface, such as a metallic surface, or from total internal reflection at the boundary between dielectrics. Sub-micron sized resonator as shown in fig. 2.2(b) uses nano- structures periodically patterned on the scale of resonant optical wavelength, for instance a planar multilayer Bragg reflector with a high reflectivity, or a photonic crystal. Semiconductor microstructures are of many kinds [25] as shown in Fig. 2.3.

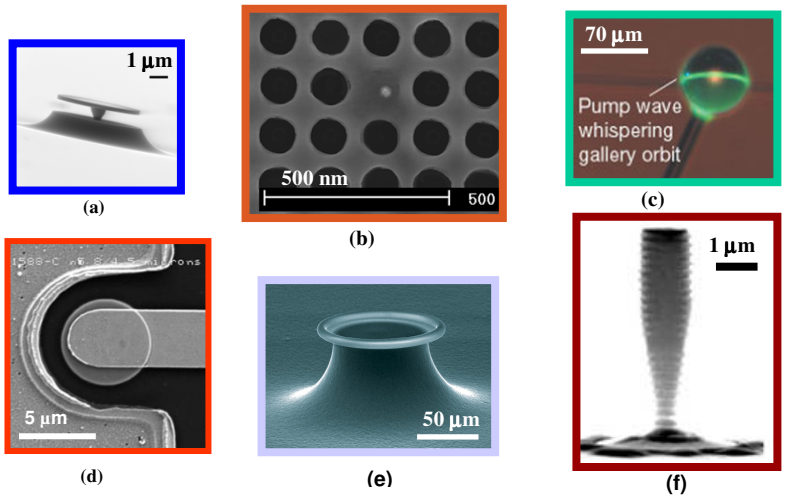

Figure 2.3 (a) Microdisk resonator [44] (b) Photonic crystal resonator [45], (c) Micro sphere resonator [46], (d) Electrically pumped microdisk resonator [47], (e) Micro toroid resonator [48], (f) Micropillar resonator [49]

Semiconductor microcavities are characterised by their properties like Quality- Factor (Q-Factor) and the effective small volume to confine light as shown in the Table 2.1

Geometry	**Material**	**Q**	$V_{eff}((\lambda/n)^3)$ **µm³**	**Reference**
Fabry-Perot	Air (w/dielectric mirrors)	10^9	10^5	[50]
Microsphere	SiO_2	10^9	10^4	[51]
Micropillar	GaAs/AlGaAs	2×10^3	5	[52]
Microdisk	GaAs/AlGaAs	1.2×10^4	6	[53]
photonic crystal	InP/InGaAsP GaAs/AlGaAs	500 2.8×10^3	0.3 0.4	[54]

Table 2.1 Q and V_{eff} for several experimentally demonstrated semiconductor microcavity structures

The Q- factor is a measure of the rate at which optical energy decays from within the cavity (from absorption, scattering or leakage through the imperfect sidewalls of the microcavity) and where Q^{-1} is the fraction of energy lost in a single round- trip around the cavity.

The semiconductor microcavities shown in Fig. 2.3 (a), (c), (d) and (e) have the capability of confining the light and lase in the plane of the device. QDs present in the active region of the microcavity provide optical gain to support lasing into a whispering gallery resonance. Devices based on semiconductor microcavities have wide area of applications. They can be used in transmitting data for long distance communications [55]. They can be used as a read-write laser in CD and DVD players. Microcavities can also be used as a highly efficient logic element in quantum information processing [56].

2.1.2 Microdisk resonator

Semiconductor microcavities have generated interest as test beds for light-matter interactions such as those between excited electron spins and photons confined in a cavity [57,58].Disk cavity geometries result in many attractive qualities including relatively high *Q* factors, low lasing thresholds, and strong in-plane emissions manifest in the form of electromagnetic whispering-gallery modes [59,60]. Additionally, both weak [61] and strong [62] coupling between electrons and photons

have been observed in single microdisks containing quantum dots, providing possible avenues for quantum information processing schemes [63, 64]. Furthermore, ultralow lasing threshold has been achieved in both optically [53] and electrically pumped [47] microdisk lasers. fig. 2.4 shows a schematic diagram of a microdisk laser.

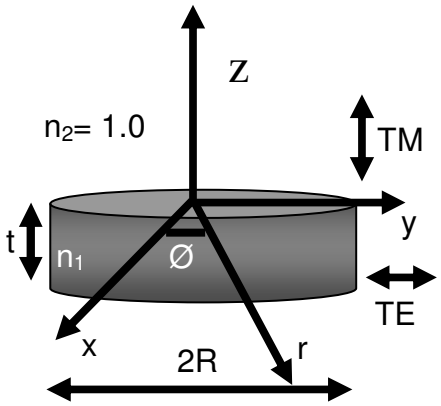

Figure 2.4 Schematics of Microdisk lasers

It consists of a thin disk of thickness *t* and radius *R* containing the active region with a refractive index, n_1. The disk is surrounded by a medium of lower refractive index, n_2. Dielectric discontinuity along the z- axis strongly confines the modes in the vertical direction, z. Total internal reflection occurs at the curved interface due to dielectric discontinuity in the radial direction, *r*, and leads to the formation of whispering gallery modes. Whispering- gallery modes

resonates with TE- polarization (electric field E lies in the x-y plane) and TM- polarization (electric field E lies along the z- axis) in a microdisk. TE- polarization have high quality-factor, Q and with no radiation losses. However due to strong contrast of refractive-index along the disk thickness, the TM-polarized modes undergo strong confinement inside the disk, and are not seen in experiment. The spatial dependence of the electric field, E in the r-ø plane for the whispering-gallery resonance of order M is $E_{N=1,M}(r,\phi) = J_M(\frac{2\pi n_{eff} r}{\lambda_{N=1,M}})e^{jM\phi}$ where J_M is a Bessel- function of integer order M. The resonant wavelength satisfies the condition that the Electric field vanishes at the edge of the disk, i.e. $J_M(\frac{2\pi n_{eff} r}{\lambda_{N=1,M}}) = 0$ where n_{eff} is the effective refractive index of the disk. Whispering- gallery modes have the first- zero of J_M occurring at r = R. In an ideal case higher- order radial modes (N > 1) show monotonic decrease in Q- factor with increasing N. The physical significance of M is that there are 2M intensity maxima around the periphery of the disk in the azimuthal direction, when it is increased from ø = 0 to 2π.

Interface fluctuated quantum dots (IFQDs) [44] in the active region provide optical gain to support lasing in a whispering gallery mode. The lasing emission occurs in the plane as shown in Fig. 2.5.

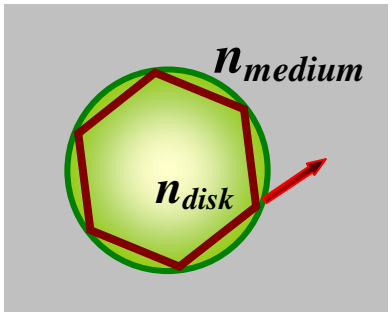

Figure 2.5 lasing emission occurs in plane

The resonant wavelengths have two fold degeneracy for the clockwise and counter- clockwise propagating modes.

2.1.3 Coupled Microdisks- Photonic Molecule

Microdisk laser (MDL) shows strong optical confinement of light due to total internal reflection results in inefficient power output [65, 66]. Things change when two or more MDLs are placed adjacent to each other. Two microcavities are electromagnetically coupled (e.g., via a finite-width air gap as shown in Fig. 2.6. This means that MDLs are coupled by evanescent waves. The extent of evanescent coupling has been shown in Fig. 2.7. Due to operating in the electromagnetic near-field region, the coupling distance of the devices should not be more than about a quarter wavelength of the cavity modes.

Figure 2.6. A pair of coupled microdisk- Photonic Molecule

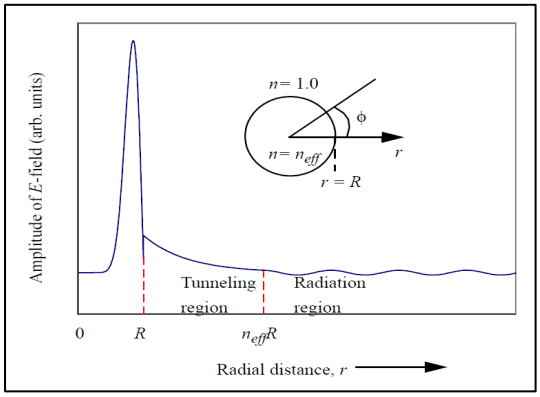

Figure 2.7. Electric field profile of a single microdisk [67]

To address some of the issues present in single microdisks such as inefficient power output and

lack of emission directionality [65, 66], arrays of microdisks coupled via the evanescent electric field at the disk edges have been proposed and fabricated [68]. These coupled states are observed in a variety of cavity geometries [68-70] where the individual electromagnetic modes blend to form "photonic molecule" (PM) modes, much like the atomically shared electronic states in a hydrogen molecule. The combination of two hydrogen atom 1s wave function forms the symmetric wave function ψ_s and antisymmetric wave function ψ_A [74] as shown in Fig. 2.8 (a) and (b)

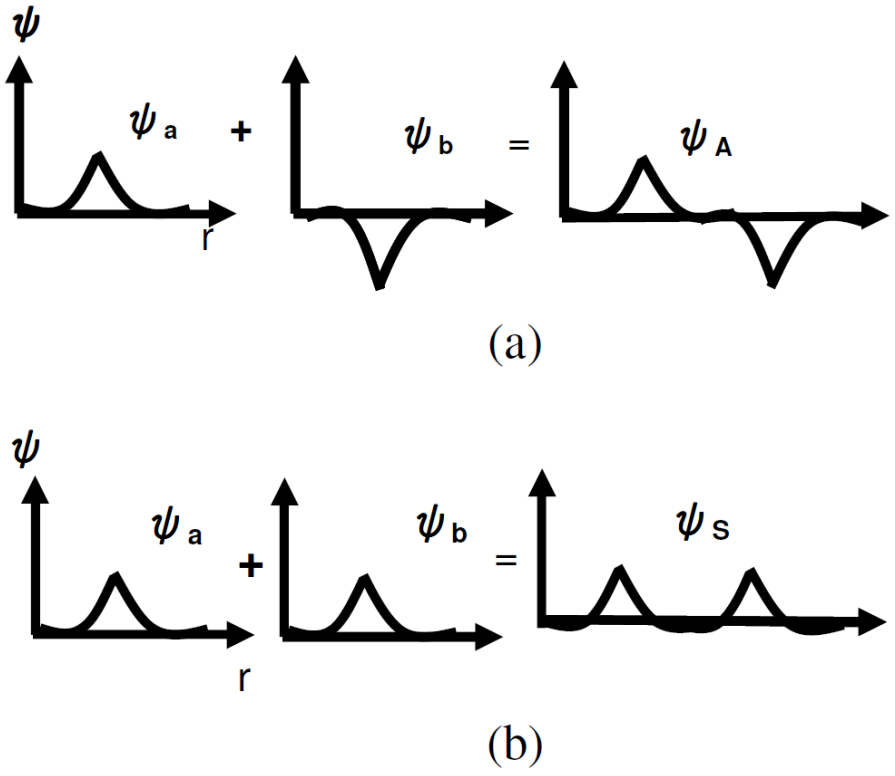

Figure 2.8 Formation of (a) Antisymmetric (b) Symmetric wave function in Hydrogen molecule

Similarly non-degenerate individual cavity modes couple evanescently and split into two bonding and anti-bonding modes. The high index contrast ratio between a whispering gallery

mode microdisk laser and its surroundings means that the lasers have high-Q values. This enhances reflectivity and mode selectivity of the Microcavity, and hence it is valid to adiabatically eliminate all variables except the field mode. Therefore, the coupling is between two single mode lasers.

In the present we investigate the PM states formed in coupled circular and elliptical microdisks using high resolution static and dynamic optical spectroscopy techniques. We observe bistable lasing of selectively coupled emission modes and demonstrate that the bistability is controllable by the incident excitation polarization. This polarization control gives us an all-optical and noninvasive means of manipulating the hysteretic emission intensity of the coupled system.

2.1.4 Experimental details

Coupled elliptical microdisks are fabricated with GaAs/ AlGaAs heterostructures and were grown by using molecular beam epitaxy (MBE) [75]. Each microdisk has an active region consisting of six 4.2 nm GaAs quantum wells with interface- fluctuation quantum dots, similar to previous studies [75, 76]. Elliptical microdisks have a minor axis length of 2 μm and an aspect ratio (minor axis/ major axis) of 0.75, and the disks are 110 nm thick. These elliptical microdisks are coupled along their major axis.

The devices are optically pumped using cw laser with emission wavelength of 532 nm. The sample was mounted in a continuous flow cryostat and cooled down to 10 K. The laser is focused down sample surface through a 100X objective, which also collects photoluminescence from the sample as shown in the Fig. 2.9

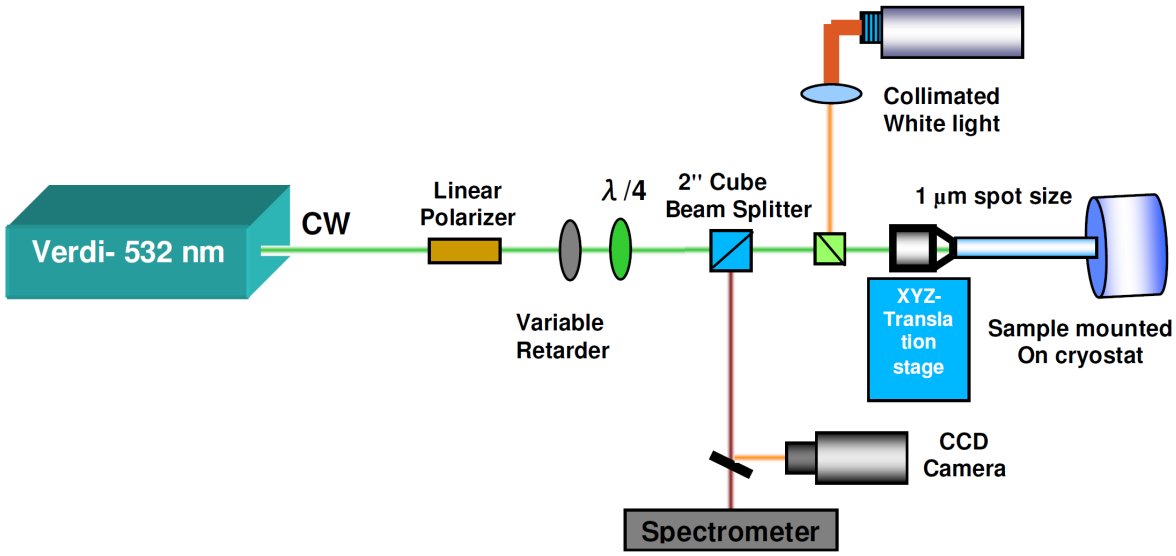

Figure 2.9 Experimental setup for low temperature photoluminescence measurements

The devices are optically pumped in three ways, as shown in the Fig. 2.10 with a flexibility of rotating the incident beam polarization.

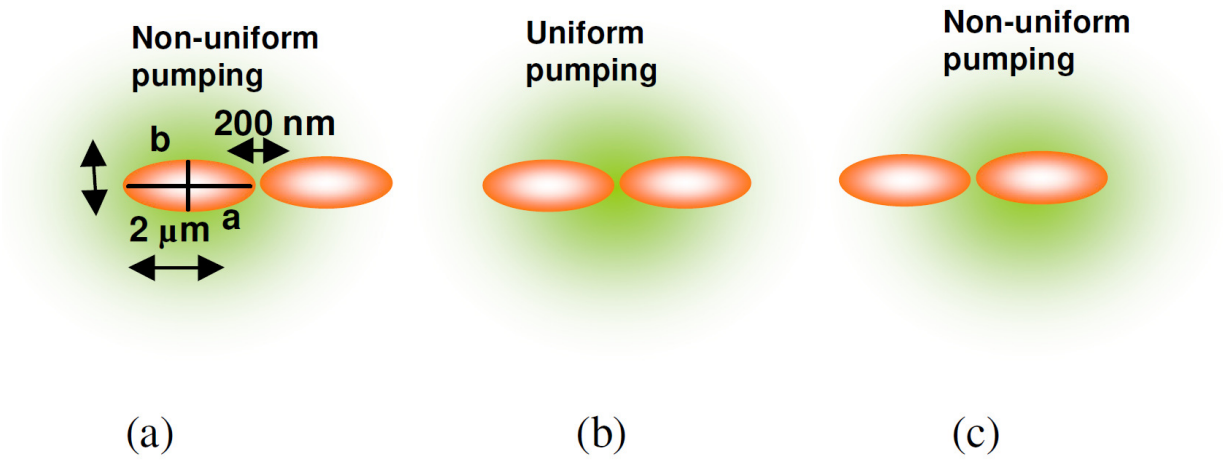

Figure 2.10. Shows illumination schemes of the disks, with the focused beam centered on (*a*) left-disk uniformly and exciting partially the right disk, (*b*) both disks uniformly illuminated, and (*c*) only the right disk is excited uniformly with partial excitation of the left disk.

2.1.6 Results and Discussion

We begin by studying coupled circular disks Fig.2.11 (a). To allow efficient mode coupling, the interdisk distance is nominally designed to be 200 nm, well within the regime of evanescent decay [60, 69]. Figure 2.11(b) shows the emission from the coupled modes at temperature T=20 K. The individual emission modes of each cavity are replaced by two resonant modes labeled bonding "b," lower energy and antibonding "ab," higher energy. In an efficiently coupled system, neither mode is localized on any particular disk [66].In reality however, no two disks are identical, which gives rise to a detuning in individual mode energies. When this detuning is small compared to the coupling strength of PMs, the modes are highly delocalized between both disks. Spatially resolved photoluminescence (PL) measurements [Fig. 11(c)] demonstrate that the disk detuning is not negligible, with the bonding mode almost entirely localized in the left disk Fig.2.11(c), top and the antibonding mode in the right disk Fig.2.11(c), bottom. This detuning is likely caused by an unintentional diameter mismatch between the pair [72].Time-resolved PL corresponding to these emissions is shown in Fig.11(d).Alteration of carrier dynamics is usual when a system crosses over from spontaneous to stimulated emission at its resonance. The typical signatures include reduction in the carrier recombination time and the "delay time," defined as the time required for the emission to reach its maximum intensity. For this disk pair, the bonding (antibonding) recombination time of 120 ps (90 ps)are much shorter than the nonresonant emission time of 400 ps. The delay time of the antibonding mode is also shorter than the bonding mode and nonresonant PL delay times. These dynamical signatures indicate that the antibonding mode has a higher Q, attributed to this mode's electric field having deeper penetration in the interdisk gap.

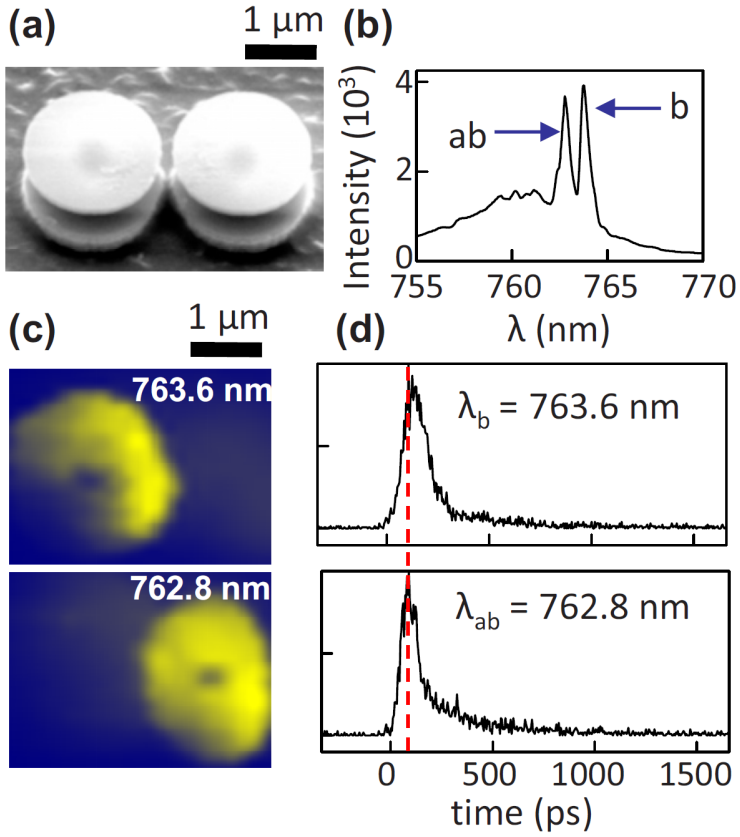

Figure 2.11. (a) Scanning electron microscopy (SEM) image of coupled circular disks. (b) Spectral emission showing coupled modes at T=20 K. The modes are labeled as bonding ("b") and antibonding ("ab"). (c, top) Spatially resolved PL scan at 763.6 nm, the bonding mode emission.(c, bottom) Similar scan centered on the antibonding mode wavelength of 762.8 nm. (d) Time-resolved PL for the two modes. Dashed line compares the two denotes the "delay times".

For this disk pair, the bonding (antibonding) recombination time of 120 ps (90 ps) are much shorter than the nonresonant emission time of 400 ps. The delay time of the antibonding mode is also shorter than the bonding mode and nonresonant PL delay times. These dynamical signatures indicate that the antibonding mode has a higher Q, attributed to this mode's electric field having deeper penetration in the interdisk gap.

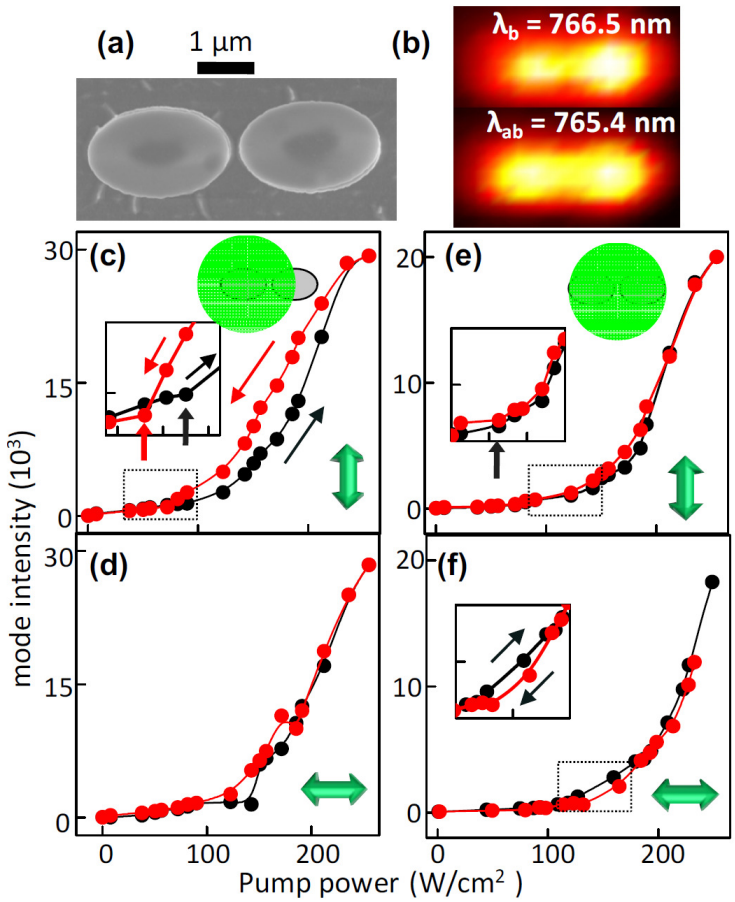

Figure 2.12. (a) SEM image of coupled elliptical microdisks. (b, top and bottom)Spatially resolved PL scans at T=10 K. The bonding mode (top) is slightly localized in the right disk, while the anti-bonding mode (bottom) is highly delocalized. (c) Nonuniform pumping (schematic) with P=90° (double-headed arrows denote polarization state). Hysteresis is observed as the excitation power is first increased in steps and then decreased. Inset highlights the lasing threshold as the power is ramped up and down. (d) Non-uniform pumping with P=0° (e) Uniform pumping with P =90°. Inset shows unchanged threshold for both branches. (f) Uniform pumping with P=0°. Magnified region in inset shows slight thermal hysteresis.

Elliptical microdisks break the cylindrical symmetry of their circular counterparts. Fortunately, prior measurements on single elliptical disks [68] have shown that at least in the weak deformation limit of aspect ratio ≥0.75, the basic nature of whispering gallery modes is not destroyed. Evanescent fields are more prominent near the larger curvature regions of an elliptical disk which enhances the coupling between an elliptical disk pair in the geometry studied

[Fig.2.12(a)]. This enhancement is observed in Fig. 2.12(b) by the more delocalized bonding (top) and antibonding (bottom) mode profiles. Our measurements indicate that PMs composed of coupled elliptical disks show stronger coupling and more equitable spatial mode distributions than the circular PM samples, which leads us to investigate the possibility of bistable operation in these coupled systems. Bistability and mode-switching, driven by the phenomenon of saturable absorption, have been observed in a variety of semiconductor microcavities. The first proposed bistable laser [77] was based on nonlinear absorption resulting from inhomogeneous current injection in a two-segmented laser. Several studies have been done on phenomena of bistable operation in semiconductor lasers with a variety of schemes including inhomogeneous current injection [78] in multisegmented structures [79] and optical injection [79]. In optically excited cavities such as ours, this is attained easily by nonuniform pumping of the coupled pair [72], as shown in Fig. 12(c). The preferentially pumped disk provides the gain while the partially pumped disk forms the loss region.

Figure 2.12(c) follows the emission intensity of the antibonding mode as a function of pump power at T=10 K. With the incident excitation polarization perpendicular to the coupling axis, (denoted P=90°) significant hysteresis is observed between the incident power ramping up and down when preferentially pumping only one disk. The anticlockwise nature of the hysteresis loop signifies that this is not a thermal effect. The inset shows that saturable absorption may be the cause as the lasing threshold is lower on the ramp down (75 W/cm^2)than on the ramp up (90 W/cm^2). This threshold reduction is consistently observed in multiple samples in the range of 15–20 W/cm^2. Repeating the same measurements under orthogonal polarization [P=0°, Fig.2.12(d)] surprisingly reveals no bistability. When uniformly pumped [Figs. 2.12(e) and 2.12(f)] there is no carrier density differential in the coupled system, and therefore, bistability is

not expected. The small clockwise hysteresis under uniform pumping [Fig. 2.12(f) inset] is the incorrect direction and is likely due to thermal effects. The same measurements in circular coupled disks do not exhibit hysteresis with either polarization while the effect shows up very reproducibly in the elliptical disks. In elliptical disks coupled along the minor axes there is a hint of hysteresis with P=0° but not P=90°. This suggests the polarization dependence of bistability may follow the geometry of the elliptical cavity rather than the axis of coupling. It may be that the different pump polarizations relative to the major axis of an individual elliptical disk spatially excite carriers across the area of the disk in different ways. It would then not be surprising to see a change in emission dynamics if this spatial extent of gain was really varying with polarization because the coupling between a carrier recombination event to a specific cavity mode is highly dependent on position within the disk. Carrier diffusion and lifetime may then further enrich this gain structure effect, contributing to the observed polarization dependence of bistability in these disks. As a check, the magnitude of emission intensities of the elliptical disks do not show a marked difference under P=0° or 90°; suggesting that the overall number of excited carriers in these disks is insensitive to the polarization despite the difference in observed dynamics. In the continuous wave measurements where the polarization dependence is observed, it is difficult to measurements. The many degrees of freedom involved in coupled cavity dynamics make this emission modulation a complicated phenomenon whose complete understanding will require rigorous analytical and numerical treatment.

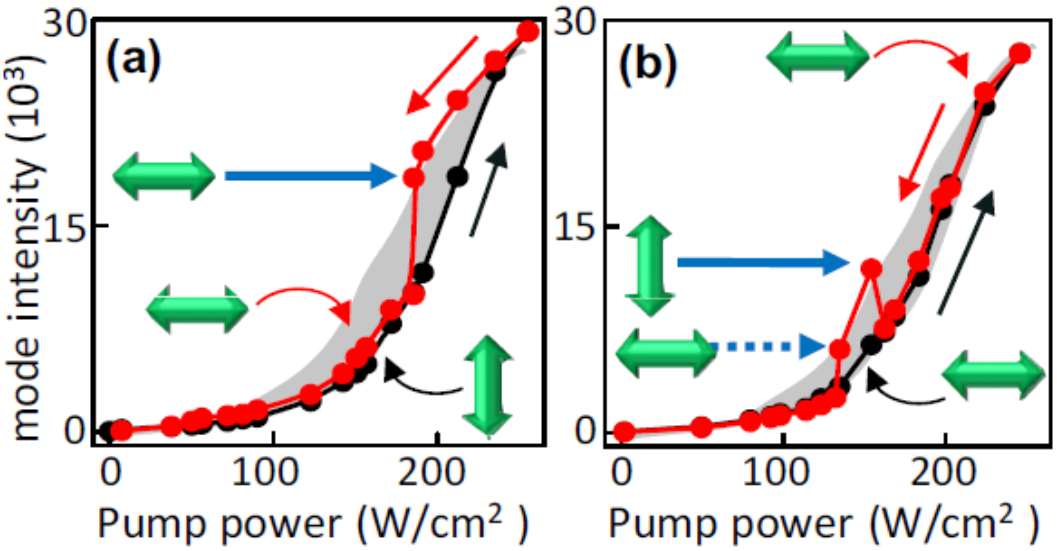

Figure 2.13.(a) Excitation signal power is stepped up with P =90°. At the power corresponding to the point on the ramp down curve highlighted by long bold arrow the polarization is switched (P=0°). Shaded area is the hysteresis curve of Fig. 2.12(c), shown for comparison. (b) Excitation is ramped up with P=0°, ramped down with P=0°, switched to P=90° (solid arrow) at 152 W/cm^2 and switched back to P=0° at 134 W/cm^2 (dotted arrow).

However, our results so far do allow us to control the mode emission bistability by changing the incident polarization. In Fig. 2.13(a), the excitation power is ramped up with P=90° on nonuniformly pumped elliptical disks. The excitation power is then ramped down with P=90°, but switched to P=0° at a midway point, (bold arrow). The hysteresis disappears and mode intensity follows the lower branch as the feedback between the two disks is

diminished. The shaded gray area is the hysteresis curve of Fig. 2.12(c) shown for comparison. In Fig. 2.13(b) we toggle the system between the two emission intensity states through polarization control. The excitation is ramped up with P=0° until the emission intensity begins to saturate, then ramped down and switched to P=90° (solid arrow) at 152 W/cm^2. The emission intensity jumps up to the value it would have had if the coupled system had achieved gain saturation at higher powers. It does not enter into this state irreversibly—switching to P=0° at 134 W/cm^2 (dotted arrow) brings the emission intensity back down to the lower branch.

Bistable behavior in semiconductor microcavities has long been viewed as a viable option for designing optical memory devices and fast switches. The switching speed in a single microcavity can easily achieve gigahertz bandwidth. In a coupled system this speed would be limited by the time scale of gain saturation, and the recombination time of the carriers in the active region. Based on measurements and theoretical estimates [80, 81] both these time scales can be as short as tens of picoseconds in a system such as ours, opening up possibilities for developing coupled arrays of ultrafast all-optical, on-chip devices with low operation thresholds and small footprints. In addition to applications in photonics, our results have important implications for solid state quantum information processing schemes centered on cavity quantum electrodynamics effects. In individual microdisks the quantum dot electron spins couple to the cavity modes. The coupled modes would allow scaling this electron-photon coupling across arrays of cavities and the switching protocol established here could potentially be developed into a means of manipulating spin coherence in such a multibit system.

2.1.7 Future Work and its importance

Photonic molecules (PMs) hold the promise of new insights into the physics of light-matter interactions. One of the primary motivations for applied research in optical bistability is its potential for optical computers and optical signal processing system.

The future work of this experiment will be mainly based on the study of controlling the optical bistability, mostly by modifying the input beam conditions, which help us to understand processes like non-linear saturable absorption, and details of other complex processes involved in carrier-induced refractive index change which might lead to effective and better modulation of mode switching effect.

Present day state-of-the-art electronic systems contain astronomically large number of interconnected basic units: switches, logic-gates and memory elements (flip-flops) which are based on bistable circuits. However, these systems consume a huge amount of power to operate the circuit and device interconnects take up a large amount of that power. Furthermore all these circuit components are based on indirect band-gap semiconductors like silicon, which has very low carrier mobility.

To overcome these problems, bistable coupled microdisks based on III-V (high carrier mobility) semiconductors are expected to be the key components in future optical communication and switching systems because of their inherent advantages such as high optical gain, low lasing threshold, and carrier induced modal refractive index changes, and saturable absorption. By proper coupling of MDLs, the emission of the MDLs can be polarized and it can be coupled to the other set of coupled MDLs. They can work as an efficient optical interconnects wirelessly as shown in Fig. 2.14.

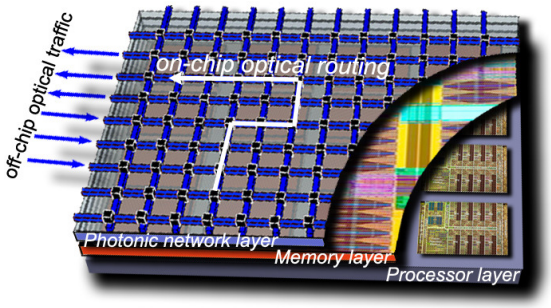

Figure 2.14 Photonic Chip [IBM research on Nanophotonics]

Due to high mobility of carriers in GaAs coupled MDLs, the switching speeds that can be reached are really high. The next generation supercomputers based on THz or higher frequency range can be made by using this kind of bistable device. Capability of switching the modes forms the building blocks of clear logic systems. The advantages of this logic include the simultaneous availability of a logic state and its binary complement, less power dissipation and better

suitability for cascading. Study of switching mechanism of cavity modes becomes an important issue. Furthermore, the ways of switching the modes and the measurement of the switching speed becomes a strong aim of this project. Switching between the normal and bistable mode of operation of these coupled MDLs are also important aspect of this project. Plans on the further studies on switching mechanisms are as follows:

Polarization based switching

Bistability can occur in MDLs if there exists a non-linear mechanism in the device that behaves as a positive feedback. The first proposed bistable laser [77] was based on non-linear absorption resulting from inhomogeneous current injection in a two-segmented laser. At that time the threshold current of semiconductor lasers was too high to be used in any practical applications. Several studies have been done on phenomena of bistable operation in semiconductor lasers with a variety of schemes, including inhomogeneous current injection [80, 81] in multi-segmented structures [79], external cavity [82] and optical injection [80]. As mentioned earlier, our experimental studies are concerned with intensity bistability involving two stable states below and above the lasing threshold. Lasing threshold measured in our devices are ultralow compared to the reported works [65, 66]. Upto now, although some studies have been done on the concept of polarized emission from MDLs [72], there has been no work on control of bistability of the cavity modes by changing the excitation polarization. This provides us with a motivation to pursue further studies on the effect of polarization modulation on bistability among coupled disks. Thus, it would be very much interesting to study and investigate the effects of excitation polarization orientation on saturable absorption at low-temperatures.It has been shown in the last section that the optical hysteresis or bistability goes on and off by switching the excitation beam polarization. In this regard, it becomes very much relevant to determine effect of switching of

incident beam polarization at incident powers above and below particular lasing thresholds of selected MDLs. A similar procedure of flipping polarization would be attempted at maximum intensity of the anti-bonding mode. The insight gained through these measurements would be beneficial in terms of device application as the knowledge assimilated would help develop physical foundation for polarization based logic with a unique advantage of offering logic state and its binary complement in tandem.

Modulation of bistability: Controlled size-mismatch of disks and variation of coupling distance

The motivation for studying interactions of optical modes in a photonic molecule with size mismatch originates from two sources. First, precise and repeatable fabrication of identical microcavities, which are few microns in diameter, is highly challenging. Second, a systematic study of coupled MDLs with various degrees of cavity size mismatch can reveal new mechanisms of manipulating their optical properties, thus paving the way to improving or adding new functionalities to PM-based photonic devices. Furthermore, strength of coupling depends on difference between the original resonant wavelengths of the MDLs being proportional to the difference in the diameters of the MDLs [65]. The strength of coupling also depends on actual inter-disk distance. This provides us an opportunity to conduct a systematic study of bistability by fine-tuning coupling distance between the MDLs. Despite its simplicity, coupled MDLs provide useful insight into general mechanism of cavity mode coupling and offers new design and ideas for more complex structures.

Pulsed laser based switching

Response time of a saturable absorber, is defined as the time required to reduce the quantity $(\alpha-\alpha_S)/(\alpha_0-\alpha_S)$ from 1 to $1/e$, is given by

$$t_r = \left[\frac{\tau_{21}}{1 + \frac{I}{I_S}} \right] < \tau_{21}$$

where α, α_S, α_0 the instantaneous, steady state, and small-signal values of the absorption coefficient, I_s is the saturation irradiance and I is excitation intensity the respectively [83], τ_{21} is the lifetime of the transition associated with the optical transition from state 2 to 1 and is related to the transition probability A_{21} by expression

$$\tau_{21} = 1/A_{21}$$

, and the recovery time of the saturable absorber is equal to the effective lifetime, which is given by

$$\tau = \frac{(2\tau_{31}\tau_{32} + \tau_{31}\tau_{21})}{(\tau_{32} + \tau_{31})}$$

where τ_{ij} are the respective lifetimes of the transitions from the state '*i*' to '*j*'.

Figure 2.15 below shows time-dependence of the absorption coefficient, where $t = 0$ is the time when the pulse excites sample, which is followed by an exponential decrease in absorption coefficient. For the case when the intensity I is a function of time, the steady state solutions of the absorption coefficient happen to be the good approximations if I does not vary appreciably within a time t_r defined above. Usually, saturable absorbers have typical effective recovery times, τ, of few nanoseconds or less [83].

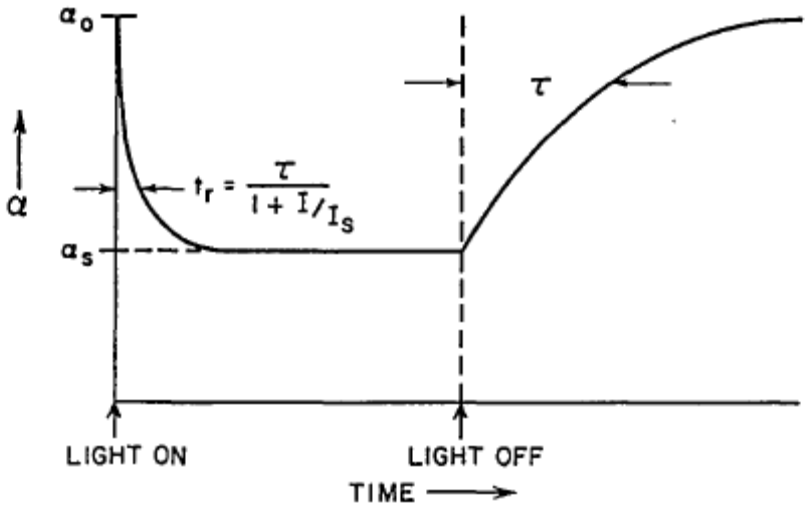

Figure 2.15. Temporal response of saturable absorption coefficient, α, to an excitation pulse [83].

Coupled MDLs excited with 100 fs wide pulses, pulse-gap of 13 ns between two consecutive pulses, fail to show hysteresis effect in them. The possible reason would be that saturable absorber is not getting saturated and it is decaying faster then the pulse gap of 13 ns. Therefore, it becomes imperative to do measurements with inter pulse-gap reduced to time-intervals approximately the same as the recovery time of investigated saturable absorber and longer pulse-widths. This sets the stage for further investigations. Time-resolved measurements using time-correlated single-photon counting (TCSPC) measurements, while use of a pulse-picker would allow us to tune the inter-pulse gaps.

Two beam based switching and triggering

It is always nice to have a triggering mechanism in device, which helps to switch the hysteresis '*on*' and '*off*' and this can be achieved using a cw beam, as mentioned in experiment. But using cw beam to achieve switching speed suffers from an inherent disadvantage in terms of maximum switching rate possible. Use of pulse beam – depending on effective recovery lifetime of

saturable absorber – would allow for a high-switch rate capability, limited only by pulse-repetition rates, which are already quite high in ultrafast pulsed lasers.

Even more, it would be interesting to see an optical transistor action in micro-disks initiated by modulation of the input beam; a transistor is a device which amplifies a (weak) input signal in proportion to the gain set by the user. The amplification action of a transistor does not show any hysteresis effect. Therefore, we might be able to use the coupled circular-disks, as these show no hysteresis in them, but have good lasing characteristics.

The transistor action from coupled circular microdisks would be achieved by using a cw beam and amplification of optical signal which is proportional to intensity of the pulsed, low-intensity input beam. Such a capability of switching amplifications at ultrafast rates would allow for realization of a fast logic system. The measurement, and possibly fine-tuning of switching time at will, would be an exciting aim for this work.

Three level or Tristable logic

Saturable absorber microdisk actually acts as a feedback element in the coupled microdisk system. It helps to maintain the bistability by self regulating the optical circuit. The present work uses two coupled elliptical microdisks. That is, it has only one feedback element. It becomes more efficient if one more feedback disk comes into the vicinity of the other two disks as shown in fig. 2.16

Figure 2.16 Schematics of two saturable absorber coupled microdisks

The aim would be to switch the coupled modes of the three coupled microdisk lasers. The experiment can be done by photopumping the center disk uniformly and partially pumping the

other two disks. Operating coupled microdisk system by this way helps to make a logic system where three level of output is possible for single input. This kind of logic system can be called as Tristable logic system.

The above mentioned switching mechanisms and its features can be adapted in Silicon photonics. That would make the next generation computing really cost effective.

2.2 Enhanced Electronic Energy Transfer in Coupled Colloidal QDs deposited on Roughened Metallic Surfaces

2.2.1 Experimental details

We start with thermoplastic substrates, which have a unique property that is characterized by their peculiar response to the changes in temperature. These thermoplastic substrates are prestressed uniaxially and biaxially following standard procedures [84]. This process is followed by sputter-coating of a 30 nm thin Gold-Palladium (AuPd) or Gold (Au) films on these prestressed substrates, and is followed by a post-deposition annealing at 160°C for 7 minutes. The process of annealing leads to development of anisotropic buckling pattern of the deposited metallic film in uniaxially pre-stressed substrates, and isotropic pattern in case of the biaxially pres-stressed substrates. Finally, commercially available chemically synthesized colloidal core-shell Cadmium-Selenide/Zinc-Sulphide (CdSe/ZnS) quantum dots (QD) of different dot sizes dispersed in toluene solutions at different concentrations were spin-coated, at 1000 rpm for ten seconds on these AuPd or Au coated substrates, to form QD monolayers.

Optical properties of these QD coated substrates were mapped spatially using static and time-resolved Photoluminescence (PL) techniques. A frequency-doubled mode-locked ultrafast Ti:Saphire laser with a pulse width of 100 fs and a repetition rate of 76 Mhz was used as a

primary excitation source, and the excitation frequency was 410 nm. A liquid-crystal variable wave-plate retarder together with a linear polarizer and a quarter waveplate were used to continuously rotate the linear polarization of the excitation beam between 0° and 90°. A 100x objectives was used to obtain a focused spot size of ~ 1 µm, and the obtained power density of the laser beam incident on the sample was 9.3 kW/cm^2. The samples were mounted on three axes motorized translational stages, which allowed spatial movement with a resolution of ~40 nm. The PL was collected in reflection via fiber and spectrally resolved by an ActonPro 2300i spectrometer (spectral resolution of 0.2 nm) on a thermoelectrically cooled CCD camera. The PL collection was done polarization sensitive along two orthogonal directions (0° and 90°). In order to do time resolved PL (TRPL) measurements, a single photon avalanche diode (SPAD) from MPD in combination with a time correlated single photon counting system (TCSPC) from Picoquant was used. The best possible time resolution of this setup was ~42 ps (detector limited). The setup of our path allowed us to perform either static or time resolved PL (TRPL) as required without major changes to be made to it.

2.2.2 Results and Discussion:

Scanning Electron Microscopy (SEM) images of both isotropic (biaxial) and anisotropic (uniaxial) metallic surfaces are shown in Fig. 2.17(*a*) and 2.17(*c*). Biaxially pre-stressed substrate, which develops isotropic metallic structures, undergoe an almost uniform spatial buckling and the underlying structure, displays a crumpled pattern and undulations, while uniaxial substrates develop anisotropic, twisted ribbon-like patterns due to highly directional (one-dimensional) buckling. The voids in the upper-right corner of the SEM image are growth related defects. Buckling of the metallic thin-films in both cases occurs due to difference in the

thermal expansion coefficients of the thermoplastic and metallic thin-film, which results in the formation of self-assembled petal-like (metallic) structures with dimensions varying from a few nanometers to tens of microns. Spatial intensity mapping of reflectance from isotropic surface is shown in Fig. 2.17(*b*). Overall reflectivity from the structure is relatively quite-low (shown by blue colored areas) but at some places sharp spikes in reflectivity can be observed, and these can be correlated

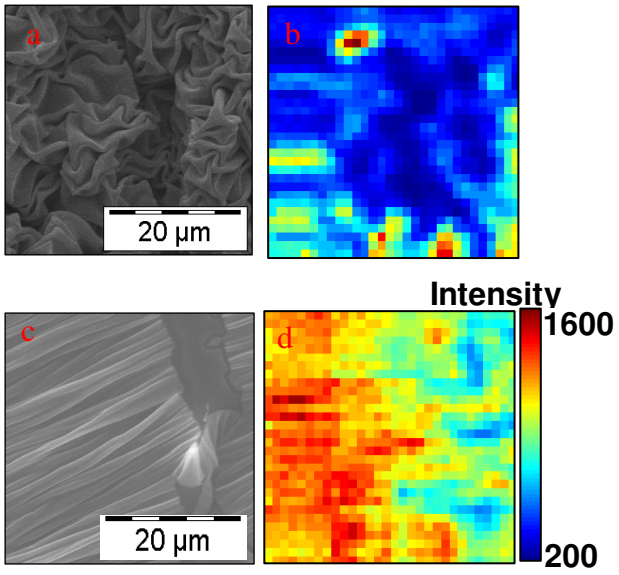

Figure 2.17: (*a*) SEM image of topographic details of isotropically structured substrate, which shows buckling of the substrate along two dimensions, underlying structure displays a crumpled pattern and undulations of the substrate where the scale-bar indicates the appropriate dimensions, (*b*) spatial intensity mapping of reflectance from the same area by scanning a focused laser beam across the samples surface, (*c*) SEM image of anisotropic substrate. In which twisted ribbon-like structure are discernible and the void seen in the upper-right corner of the image is a growth defect, (*d*) intensity mapping of its spatial dependence of its reflectance across the substrate, where it can be noticed that magnitude of reflection is about 8 times higher than that in the isotropic structure.

with the reflection from the raised parts of metallic microstructures in the SEM images. Regions of dark blue patches correspond with the regions of voids seen in the middle of the SEM image Fig. 2.17(*a*). Spatial intensity mapping of reflectance for uniaxial substrates is shown in Fig. 2.17(*d*). In this case, the microstructure has overall high reflectivity as compared to the isotropic

substrates. However, there are some places where the intensity of reflection is quite low as indicated by the blue shaded regions in the 2D scan. These areas of low reflection correlate with the underlying

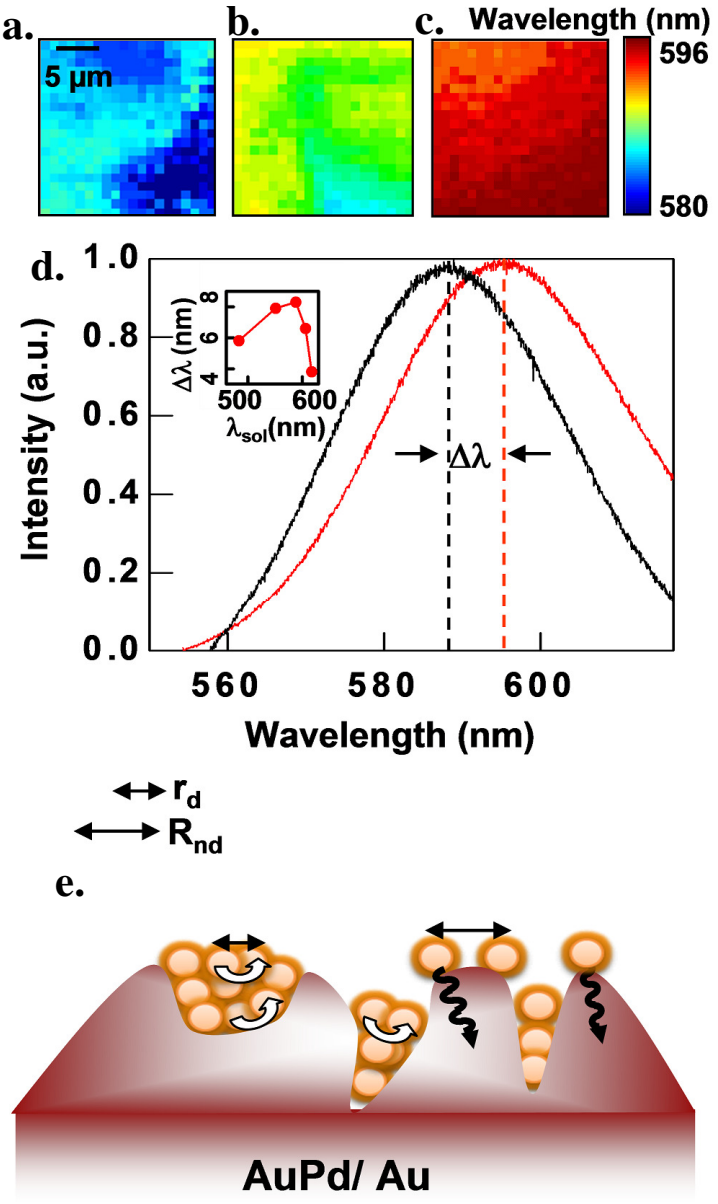

Figure 2.18: 2D mapping of PL emission from CdSe/ZnS cores-shell QDs deposited on (*a*) flat Au substrate. The QDs in concentrated solution have a peak emission at 588 nm and no red-shift of the peak-emission wavelength from QDs on these substrates is observed, (*b*) anisotropic substrate, where the peak emission wavelength shows an average red-shift ($\Delta\lambda$) of ~ 3 nm, (*c*) isotropic substrate, where a relatively large red-shift of about 8 nm occurs. (*d*) Static PL (black line) of the QDs in the solution as well as PL (red-line) from QDs deposited on an isotropic

substrate. The peak emission wavelength for the QDs deposited on the isotropic substrate is red-shifted ($\Delta\lambda$) by ~ 8 nm. The inset shows red-shift for QDs of different sizes deposited on an isotropic substrate, (*e*) schematics of the QDs deposited on an AuPd/Au isotropic substrate, showing dipole coupled QDs which undergo energy transfer, the optical signature of which is the red-shift of the peak emission wavelength of the PL. Also shown are the uncoupled QDs which quench the PL.

Spatially resolved two-dimensional map of PL emission from CdSe/ZnS cores-shell QDs with peak-emission wavelength (λ_{Peak}) of 588 nm (at concentration of 0.098 mg/mL) deposited on flat Au substrate is depicted in Fig. 2.18(*a*). Relative to emission from the QDs in solution, no red-shift of the λ_{Peak} wavelength from QDs coated on the flat-Au substrate was observed. Whereas, as shown in Fig. 2.18(*b*), the λ_{Peak} shows a relatively uniform and homogenous average red-shift ($\Delta\lambda$) of ~3 nm, in the case of QDs coated on anisotropic substrates. On the other hand, a relatively large red-shift of λ_{Peak} by about ~ 8 nm occurs for QDs deposited on isotropic substrate, and is shown in Fig. 2.18(*c*). The blue shaded region with no red-shift corresponds with the void in the middle of the image.

The λ_{Peak} of the QDs coated on flat-Au substrates does not undergo a red-shift due to the absence of spatial (corrugation) features on flat-Au surface. While, uniform red-shift (~3 nm) of λ_{Peak} coated on anisotropic substrates is because of formation of highly-ordered uni-directional (underlying) metallic structures. The one-dimensional (corrugated) structuring of metallic understructure promotes ordering of coated QDs and upto three-fold enhancement of the PL intensity because of electric field enhancement due to localized Plasmon excitation. In isotropic substrates, the underlying topographical features of the metallic surface lead to close-packing of coated QDs and hence to their enhanced spatial aggregation, the optical signature of which is the red-shift in the λ_{Peak}. Similar results were obtained for the QDs coated on both Au and Au-Pd layered thermoplastic substrates.

The red-shift(s) of λ_{Peak} of QDs coated on both anisotropic and isotropic substrates is an evidence of facile energy transfer [85] processes due to inter-dot dipole-dipole coupling among proximal dots, as the close-packing of QDs leads to stronger overlapping of their wavefunctions. However, as is well known, the degree of red-shift in λ_{Peak} is a convolution of (Förster) energy transfer efficiency as well as of the spectral inhomogeneity of the QD size.

Fig. 2.18(*d*) shows the static PL from core-shell CdSe/ZnS QDs in solution with λ_{Peak} at 588 nm in solution (black line), as well as the red-shifted PL from QDs coated on an isotropic substrate (red-line). The inset to the figure shows the degree of red-shift as we change the size of the QDs coated on an isotropic substrate. Initially, there is a relatively strong red-shift ($\Delta\lambda \sim 8$ nm) by the emission wavelength which peaks at QDs emitting at 588 nm followed by a strong decrease in $\Delta\lambda$ as larger size QDs are coated. The broadening of the linewidth for QDs coated on isotropic substrate reflects the size distribution of the QD-aggregates formed in different regions of the surface.

The illustration depicted in Fig. 2.18(*e*), shows the schematics of the QDs deposited on a AuPd/Au isotropic substrate. The QDs that are positioned physically close (r_d) together form a dipole-dipole interaction coupled ensemble that leads to well known Foerster electronic energy transfer along a chain of QDs. This energy transfer along the chain leads to delocalization of the exciton, and causes the red-shift seen in the PL mapping. However, also shown is a depiction of areas on the substrate where QDs are relatively far (R_{ND}) from one another, and therefore do not undergo dipolar-coupling. As no inter-dot energy transfer occurs in this case, the electronic excitation is ultimately transferred to the plasmons in the metallic substructure, and causes PL quenching as indicated by the wavy arrows next to isolated QDs.

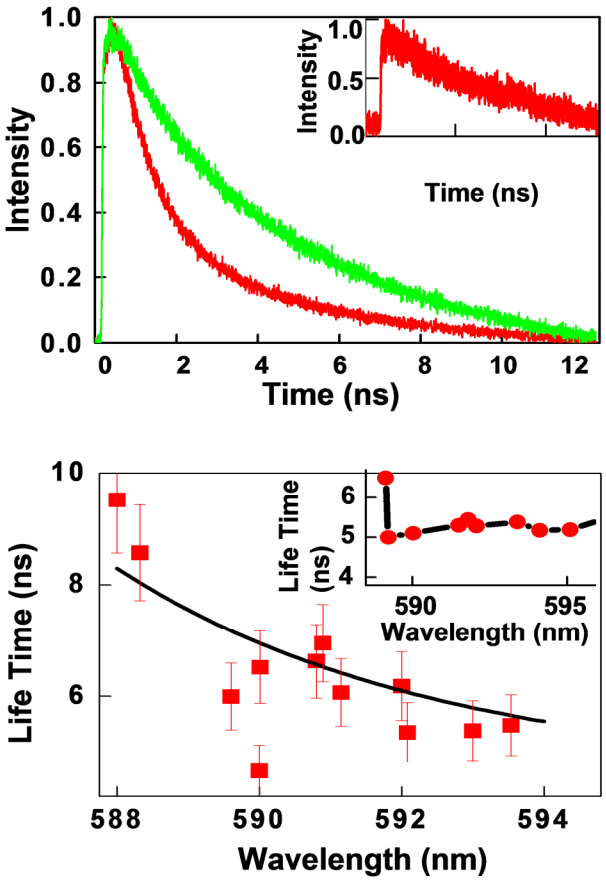

Figure 2.19: (a)Time-resolved PL (green curve) from CdSe QDs, spin-coated on an isotropic substrate, for the peak emission at 588 nm, and also for the red-shifted emission peaked at 592 nm—in the same system. The inset depicts the lifetime decay characteristics of the same QDs in solution (τ_1 = 11 ns), (*b*) and peak-emission wavelength dependence of the radiative lifetimes (τ_1), which displays an exponential (decreasing) trend of lifetime with increasing peak emission wavelength. Inset shows that decay lifetimes show almost no variation for different peak-wavelengths, for the QDs coated on a flat-Au substrate.

Fig. 2.19(*a*) shows the time-resolved PL (green curve) from CdSe QDs coated on isotropic substrate with λ_{Peak} ~ 588 nm, and also for the red-shifted emission (λ_{Peak} ~ 592 nm). The lifetime(s) for the λ_{Peak} ~588 nm, as determined from single-exponential fit to the experimental curve, is ~ 9.5 ns, while that for the emission at ~ 592 nm were τ_1 = 4 ns, τ_2 = 1 ns, τ_3 = 0.55 ns. The inset to this figure depicts the lifetime decay characteristics of the same QDs in solution, where the QDs have a radiative decay lifetime of about 11 ns. It is clear that the fast decay components τ_2 and τ_3 are observed only in red-shifted regions. The obtained results imply that

the 1-ns decay component is due to the energy transfer between the QDs and the fastest decay component of 0.55 ns is due to the energy transfer from QDs to plasmon is metal. Furthermore the radiative decay component τ_1 in the red-shifted regions and the regions where the QDs have λ_{Peak} ~588 nm is highly reduced showing the close-packed nature of the QD monolayer on isotropic surface.

The fig. 2.19b shows that as we shift towards higher wavelengths, the lifetimes (τ_1) show a general decreasing trend (8 ns to 4.5 ns), while the inset shows for the case of the QDs deposited on flat-Au substrates shows that there is no general trend in the decay lifetimes τ_1 as we move from smaller wavelength region to higher wavelength regions.

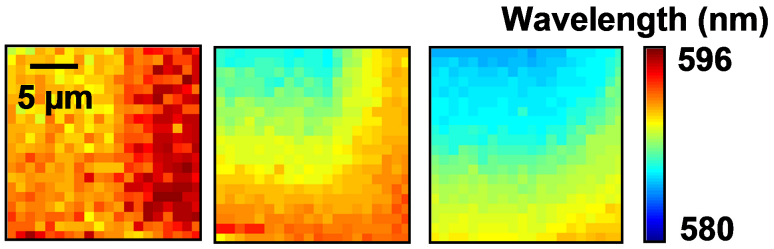

Figure 2.20: Spatial distribution of the PL from highly diluted QDs coated on isotropic substrate with a concentration of (*a*) 0.003391521 mg/mL. The PL from this sample shows a nearly uniform red-shift of 8 nm, (*b*) 0.002262895 mg/mL, where the QDs peak emission shows a non-uniform red-shift over the scanned area, (*c*) 0.001358641 mg/mL. In this case, an even more inhomogeneous red-shift, $\Delta\lambda$ ~ 2 nm or less is seen.

In order to further understand the observed red-shifts and modified emission line-shapes, a serries of QD dilution dependent PL studies were undertaken. Fig. 2.20(*a*) shows the spatial distribution of the PL from QDs (λ_{Peak} ~588 nm) of concentration 0.01246 mg/mL (1:400 by volume) spin-coated on isotropic substrates. A nearly uniform red-shift of ~ 8 nm is seen throughout the scanned area. On the other hand, Fig. 2.20(b) shows PL from the QDs diluted to even lower final concentration of 0.00832 mg/mL in solution (1:600 by volume). Here, the red-

shift is not seen to occur uniformly as was in the previous case, as there are also some areas where no red-shifting of the λ_{Peak} is seen to occur. However, even more substantial spatial PL characteristics are seen when the QD concentration is diluted to 0.0045 mg/mL (1:1000 by volume). In this case, red-shift occurs (in-homogeneously) on a very small spatial scale and by relatively minute amount ($\Delta\lambda$ ~ 2 nm or less). As the concentration of coated QDs was decreased, a consistent decrease in the degree of red-shift of λ_{Peak} of PL spectra is seen. The λ_{Peak} for QDs spin-coated on substrates approaches the λ_{Peak} values for QDs (~ 588 nm) in solution at the lowest concentrations accompanied in parallel by narrowing of the emission linewidth. As the inter-dot distances increase with decreasing concentration of QDs, the blue-shift in the λ_{Peak} with increasing dilution levels confirms that the red-shift of λ_{Peak} seen earlier occurs due to (measurable) inter-dot Förster energy transfer process.

Chapter 3

Core/Shell Heterojunction NWs prepared by LPNE

3.1 Motivation

Synthesis of hybrid nanostructures, which are composites of multi-materials, is an emerging field of material sciences attracting great deal of attention and interest. This technique provides an ability to effectively combine desirable properties of different materials to form novel nano-structures and holds the potential of creating next generation of devices and sensors. The rational design of such heterostructures can lead to novel functionalities that are independent of the individual components and may be tailored to fit a specific application. An appropriate combination of two or more metals with semiconductor NWs – which show a maximum absorption in the visible region of the solar spectrum – would serve as promising materials for applications in photoelectrochemical based solar cells.

Novel "engineered" heterostructure nanomaterials provide unique solutions critical for the harvesting of solar radiation and conversion to electrical energy (solar cells). Possibility to exercise precise control over the size, shape, composition, and spatial orientation during the growth process gives rise to combination of different functionalities and advanced properties that are absent in single-component materials.

Solar cells are most promising candidates for clean and renewable energy sources [86, 87] and miniaturization of these devices would provide a potential for integrated power sources for nano-electronic systems. NWs represent a general approach to reduce both cost and size and to improve efficiency in photovoltaics [86-102]. Experimental results have shown that use of NWs

leads to an improvement in charge collection efficiency in solar cells [86-102]. Moreover, recent theoretical studies have indicated that coaxial NW structures could improve carrier collection and overall efficiency with respect to single-crystal bulk semiconductors of the same materials [86-90]. However, solar cells based on hybrid nano-architectures suffer from relatively low efficiencies, poor stabilit and high synthesis cost/complexity. In addition, previous studies have not yet addressed their use as photovoltaic power elements in nanoelectronics.

Coaxial, heterostructured semiconductor NWs (1D) attract a great deal of interest due to their unique physical properties as well as their potentially wide applications in electronic, optical structures and devices [103-104]. Currently, $CuInSe_2$ (CIS) is considered an important compound semiconductor material for use in solar cells. An advantage associated with CIS in solar cells is that CIS related materials have the highest reported power conversion efficiency (~19.5%) among all the thin-film solar cell technologies and can be easily doped into a p-type semiconductor [105-106]. CIS has high absorption cross-section, good bandgap match with AM1.5 [105-106].

In the present work, we describe a novel method to pattern coaxial Au/Cu and Au/CIS heterostructure NWs. The fabrication process for the growth of coaxial NW consists of two phases. In the first part, Gold (Au) core NWs are patterned on the glass substrate by lithographically patterned NW electrodeposition (LPNE) [107].

The second step in the process comprises fabrication of the heterostrucure by electro depositing Cu, CIS and PbSe shell structure on top of the Gold core NWs. The main steps of the fabrication process are illustrated in Fig. 3.1. One starts with Gold NW patterned substrate which is used as the core of the intended coaxial NW system. This is followed by electrodeposition of a NW shell

of desired material on the top of this gold NW core. In present case we electrodeposit Cu and CIS at constant potential usually known by chronoampeometry (CA).

3.2 Experimental Details

In the following we describe a novel method to pattern coaxial, Metal/Semiconductor (M/SC) and Metal/Semiconductor/Semiconductor (M/SC/SC) heterostructured NWs (NWs) on float glass substrate.

The fabrication process comprises two phases. In the first phase, Gold (Au) core NWs are grown on the templated glass substrates by LPNE method, shown in the Figure 3.1.

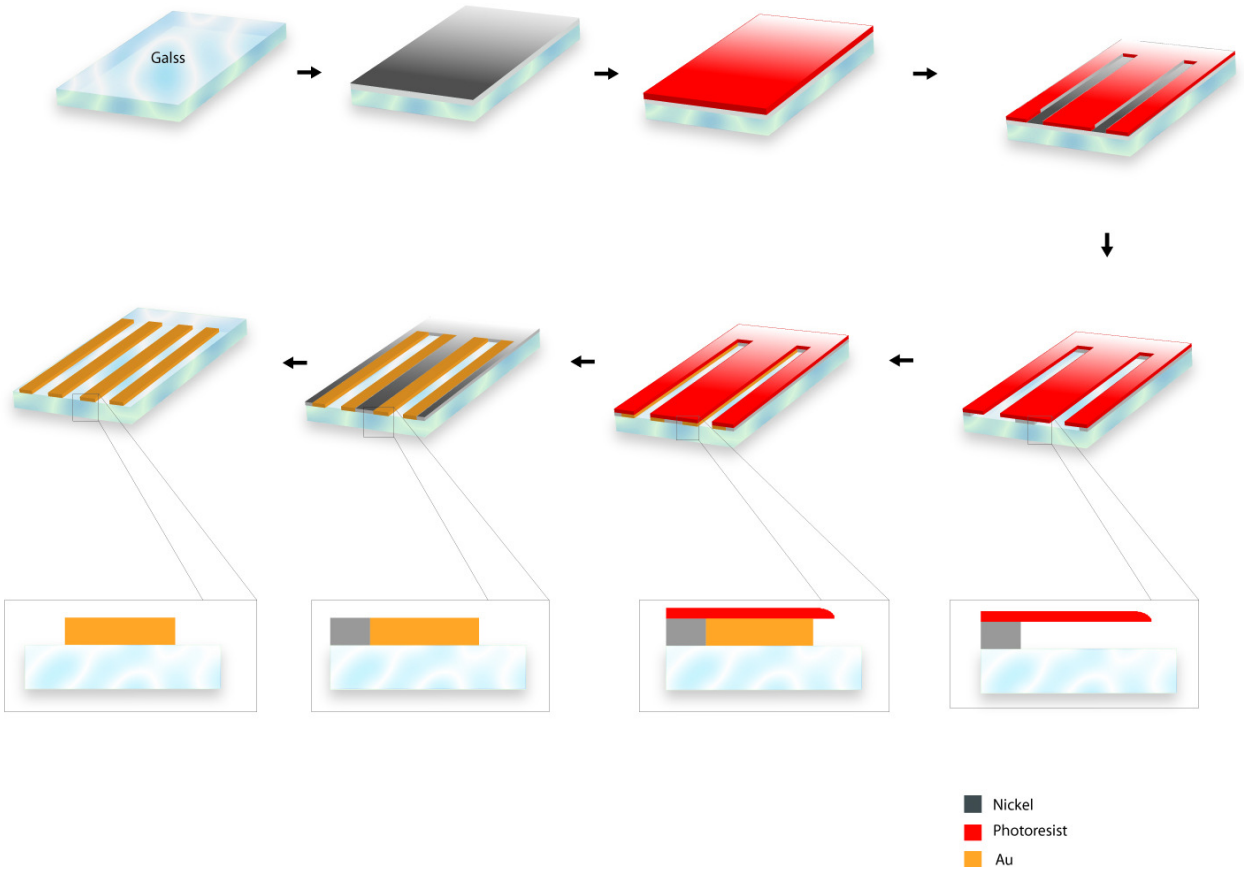

Figure 3.1. Schematics of the steps involved in the fabrication of core (Gold) NW in the first stage by the LPNE method

Lithographically patterned NW electrodeposition (LPNE) is a new method of making for synthesizing metal and semiconductor NWs on glass or oxidized silicon surfaces. LPNE is a seven step NW deposition process [107] involving photolithographically created template for NW deposition. We start with cleaning of float glass-slides (1x1 in^2) which are immersed for ~ 24 hours in a standard Nochromix solution. These are then rinsed with NANOPure water (resistivity = 18.0 $M\Omega$ cm), and dried with compressed air. Nickel evaporation, ~ 5-100 nm thick (typical values ~ 40 nm) is done by physical vapor deposition (PVD) technique using a Denton BTT-IV evaporator at 0.7 nm/s rate. Nickel pallets (99.995% pure) from Kurt Lesker were used as Nickel source during evaporation. In-situ thickness monitoring is used to determine the film thickness using SQM-160 film thickness monitor (INFICON).

A positive photoresist (ROHM & HAAS) was poured on top of Ni deposited slides using a dropper is then spin-coated at 2500 rpm for 125 seconds followed by hard baking for 30 mins at 90ºC. Next, a contact photopatterning using glass chrome mask with a 12 µm pitch resolution (Photosciences, Irvine) is performed under a 350 W UV (365 nm) light-source (OAI) for 3.3 seconds, and developed in a MF-24A solution (ROHM & HAAS), followed by rinsing in NANOPure water, and dried with compressed air.

These slides are then etched in 0.8 M HNO_3 solution (5 minutes). The etching duration and etchant concentration are fine-tuned to have a control on width of the undercuts created at the edge of the exposed PR (~300 nm). This leads to horizontal trench of precisely defined height equal to the thickness of the Ni layer. This gives a templated Ni electrode as a platform as seen schematically in fig. 3.1, step 4 for NW electrodeposition.

Thereafter, an Au NW is electroplated from an aqueous commercial gold plating solution (Clean Earth Solutions,Carlstadt, NJ) that was 6 mM in AuCl3 solution, pH 9.78) at a constant potential of -0.9 V vs Ag/AgCl within the trench. The width of the Au NW is function of electrodeposition time as shown in fig.3.2 The deposition was carried out using a pc controlled Princeton Applied Research (PARSTAT 2273) potentiostat/galvanostat at the room temperature conditions. PR and Ni layers are removed in the lift-off process. PR is removed by rinsing the sample with acetone and finally the Ni layer is etched by dipping the sample in a 0.8M Nitric acid bath. After the final etch process, the sample has gold NWs connected to Nickel contacts as shown in fig. 3.3

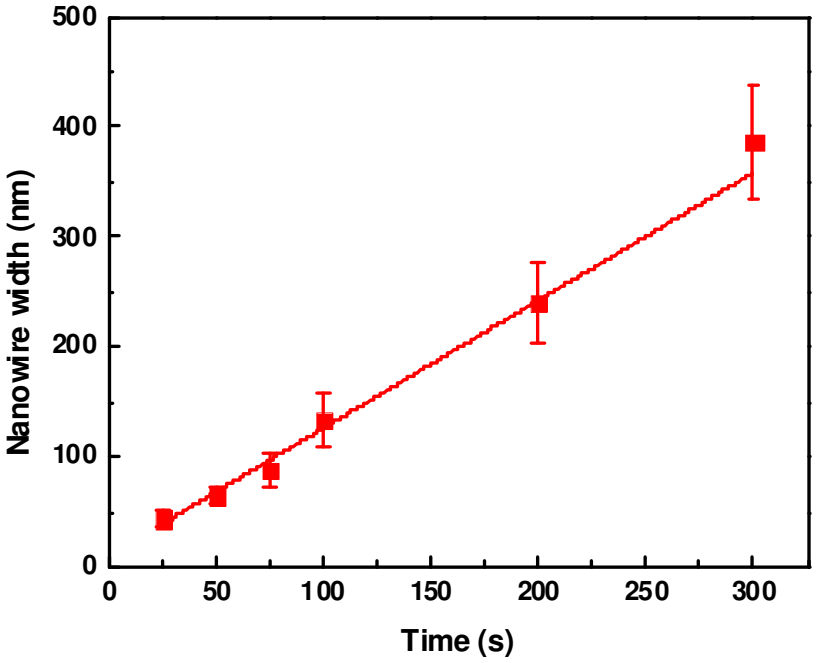

Figure 3.2 Calibration curve relating the Au NW width to electrodeposition time

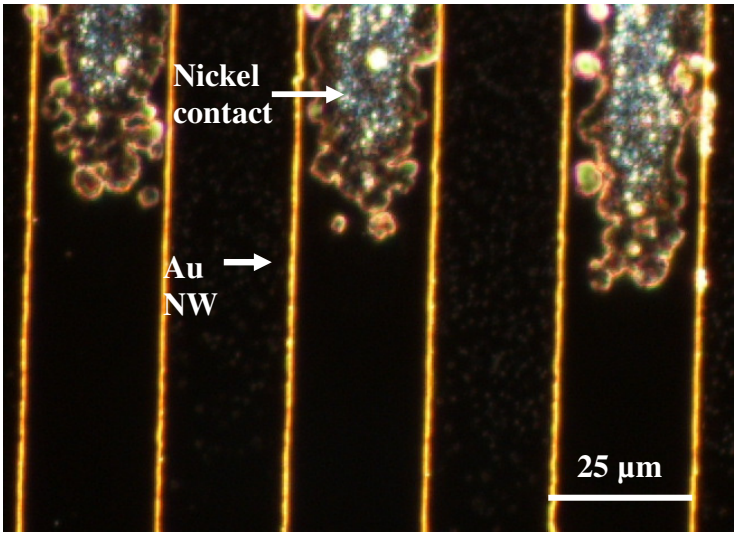

Figure 3.3 Optical microscope image at 100X maggnifictaion showing the Au NWs connected to the Nickel contacts

In the next phase, a heterostruure is fabricated by electro-depositing NW shell of selected material (Cu, CIS or CdS) over the core Au NWs from first phase.

This process is implemented by selectively etching part of the sample (step 6, Fig. 3.1) in such a way that the one half of the Au NWs have a contact with Ni metal-pad. In this way, one can forego a step which requires deposition of metal contacts to provide a electrical contact with NWs. Next, we discuss the methods for creating core-shell heterostructures in some detail.

3.2.1 Au/Cu Metal/Metal heterostructured NWs

We synthesized Au/Cu NWs by a constant potential method. In our method, Cu electrodeposition was achieved from a deposition solution containing 0.1 M $CuSO_4$ (Sigma Aldrich, Purity 99.99% metal basis), 0.4 M $(NH_4)_2SO_4$ (Fluka Analytical, Purity 99.5%), and 0.1 M EDTA (Sigma Aldrich, Purity 99%) in NANOPure water (resistivity = 18.0 MΩ cm). Metallic

Cu shell was electro-deposited on the Au core at -0.3 V versus Cu metal electrode at room-temperature (RT) conditions.

3.2.2 Au/CIS M/SC core-shell heterostructured NWs

We synthesized copper-indium-diselenide (CIS) NWs by a constant potential method following procedure used by Phok *et. al.* [108]. Fig. 3.4 below schematically shows the steps involved in CIS deposition on Au NW. In this method, CIS electrodeposition on Au core NW is achieved from a deposition solution containing 1.5 mM $CuSO_4$ (Sigma Aldrich, Purity 99.99% metal basis), 2 mM $InSO_4$ (Sigma Aldrich, Purity 99.99% trace metal basis), and 1 mM SeO_2 (Sigma Aldrich, Purity 99.999%) in NANOPure water (resistivity = 18.0 MΩ cm), with the final solution pH adjusted to 2.8 by the drop-wise addition of 1 M H_2SO_4 (Sigma Aldrich, Reagent grade). Co-deposition of Cu, In and Se is ensured between a potential range of -0.55 V to -0.7 V versus Ag/AgCl in a three-electrode cell at RT conditions without excess component deposition of Cu, In, or Se in shell NW.

To gain control over the thickness of deposited shell, a time-dependent calibration study was performed to get an understanding of the rate of deposition of the metal (M) and semiconductor (SC) shells on Au cores.

NW shells (CIS, Cu) were deposited on top of Au NW cores of three different widths (100 nm, 200 nm, 470 nm).

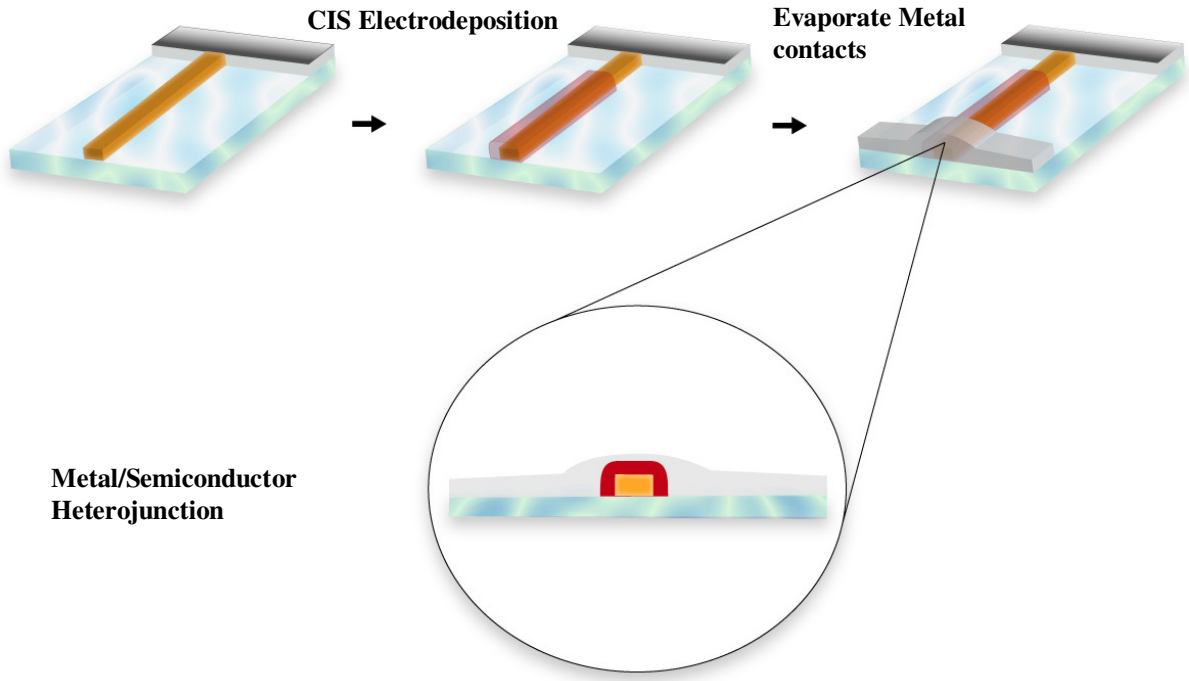

Figure 3.4. Process flow for the creation of heterostructured metal/metal and metal/semiconductor core/shell NWs

Structural Characterization:

The NWs stoichiometric ratio was characterized on a Genesis energy-dispersive X-ray (EDAX) spectrometer. The crystallographic data was collected using Scintag XDS 2000 Diffractometer high-resolution X-ray diffractometer (XRD) with Cu Kα radiation. The X-ray generator was operated at 40 kV and 40 mA.

High resolution studies of the NW morphologies were performed using field-emission scanning electron microscopy (FESEM) on a FEI XL- 30 system.

Transmission electron microscopy and selected area electron diffraction (SAED) data was attained on FEI Tecnai 12 Transmission electron microscope (TEM) operated at 120 kV. Optical imaging was done using a Nikon DS camera unit DS-L2 attached to an industrial Nikon ECLIPSE LV150 optical microscope.

Photoresponse and transport Measurements:

To characterize the dark current response of the device under test (DUT), I-V measurements were done using Princeton Applied Research (PARSTAT 2273) potentiostat/galvanostat. Photocurrent measurements were performed using commercially available Oriel (Newport Inc.) full spectrum 96000 solar simulator with white light (Xe lamp) source in AM1.5G condition. On and off behavior of photocurrent was detected by chopping the incident light using a mechanical chopper at different frequencies (50-3896 Hz). The photocurrent was amplified using a Keithley 428 PROG current amplifier in the path and signals were recorded by Tektronix oscilloscope (TEK3012C). The edge type Trigger measurements were performed at 20 MHz bandwidth to lower the noise.

Absorption spectroscopy:

Extinction spectra of the 12 μm separated NWss were performed using Varian 50 scan measurement system.

3.3 Results and Discussion

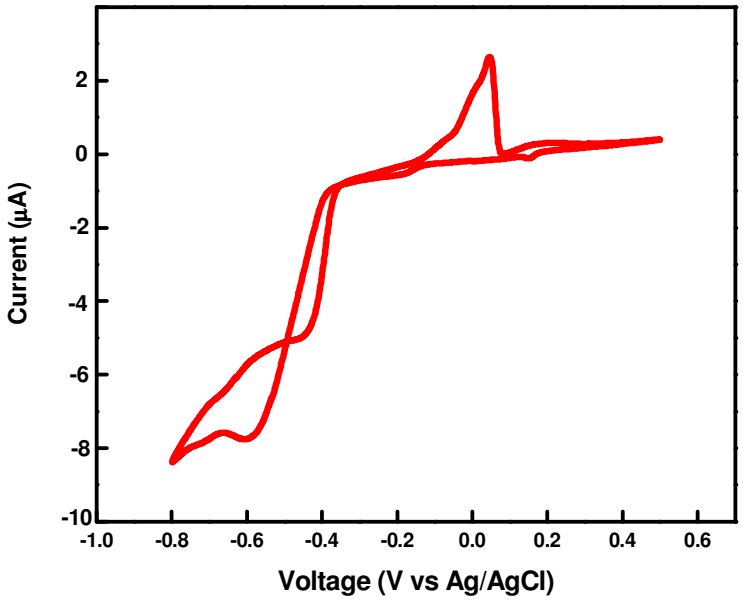

Figure 3.5. CV of the CIS electrodeposition solution.

Figure 3.5 Shows a CV of the CIS electrodeposition solution using gold NW array as working electrode. The broad peak between -0.3 V and -0.6 V vs. Ag/AgCl represents the co-deposition of copper, indium, and selenium, while the oxidation that occurs near 0.0 V vs. Ag/AgCl is oxidation of indium, copper and selenium.

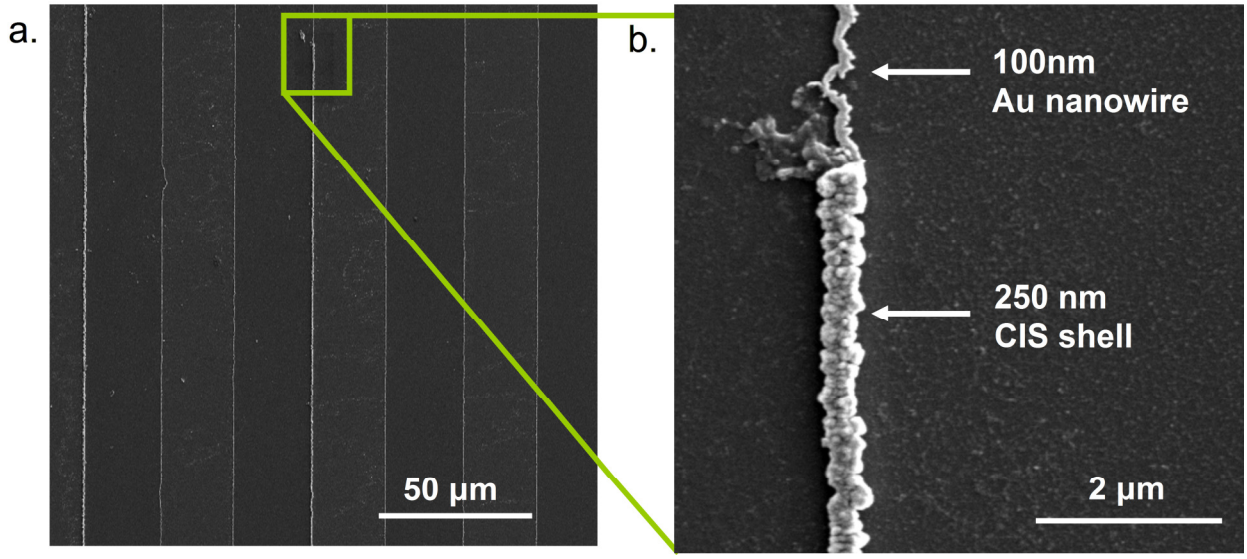

Figure 3.6. a) SEM image of arrays of Au/CIS coaxial NWs separated by 25 µm. b) SEM image showing the magnified view of a 100 nm gold NW with a 250 nm CIS shell.

The SEM image in figure 3.6a shows the arrays of gold NWs coated with CIS shell. The SEM image in figure 3.6b shows a magnified single Au/CIS coaxial NW from the same arrays of NWs as shown in figure 3.6a. It shows the single 100 nm wide gold NW which has been used as an electrode to electrodeposit CIS shell at a constant potential of -0.6 V vs. Ag/AgCl for 500 seconds in the CIS deposition solution. The gold NW, which can be seen in the top portion of the image, has been coated with approximately 250 nm of CIS. The width of the CIS shell deposition depends on both the electrodeposition time and the width of the gold NW, as the calibration curve in figure 3.7 shows. EDAX, shown in figure 3.8, reveals the presence of copper, indium and selenium in atomic percents of 27%, 28%, and 45%, respectively, close to the expected percents of 25%, 25%, and 50%.

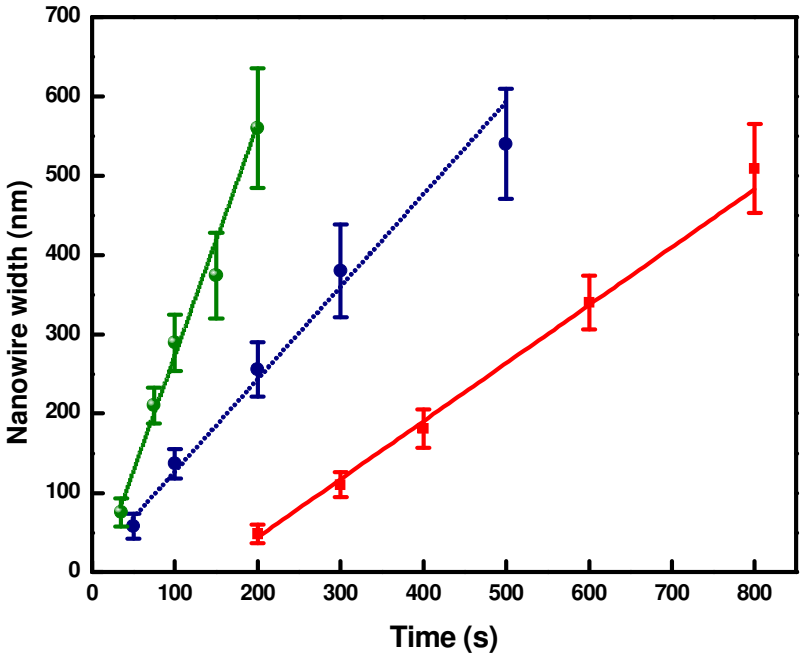

Figure 3.7. Calibration curves relating the CIS shell thickness to electrodeposition time and gold NWs widths of 100 nm (red), 250 nm (blue) and 470 nm (green) respectively.

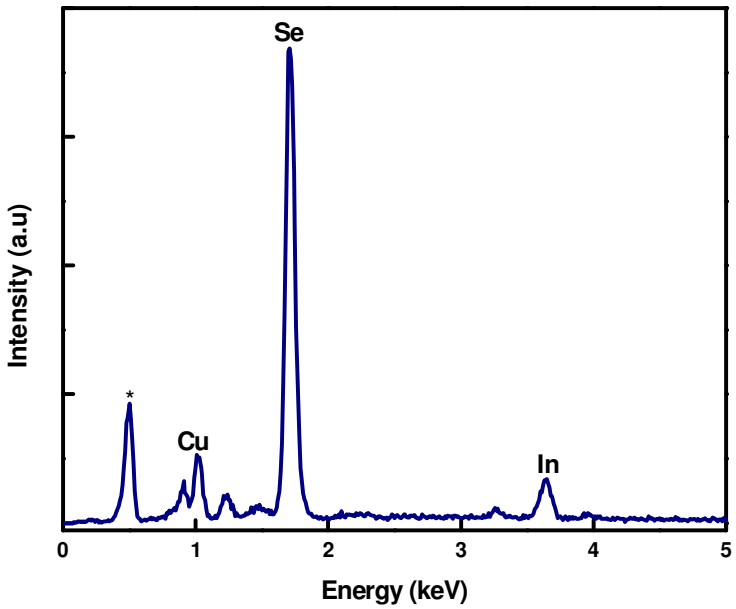

Figure 3.8. EDAX spectra of a CIS-coated gold NW showing the presence of copper, indium, and selenium. The starred peak in the EDAX spectra is from the background

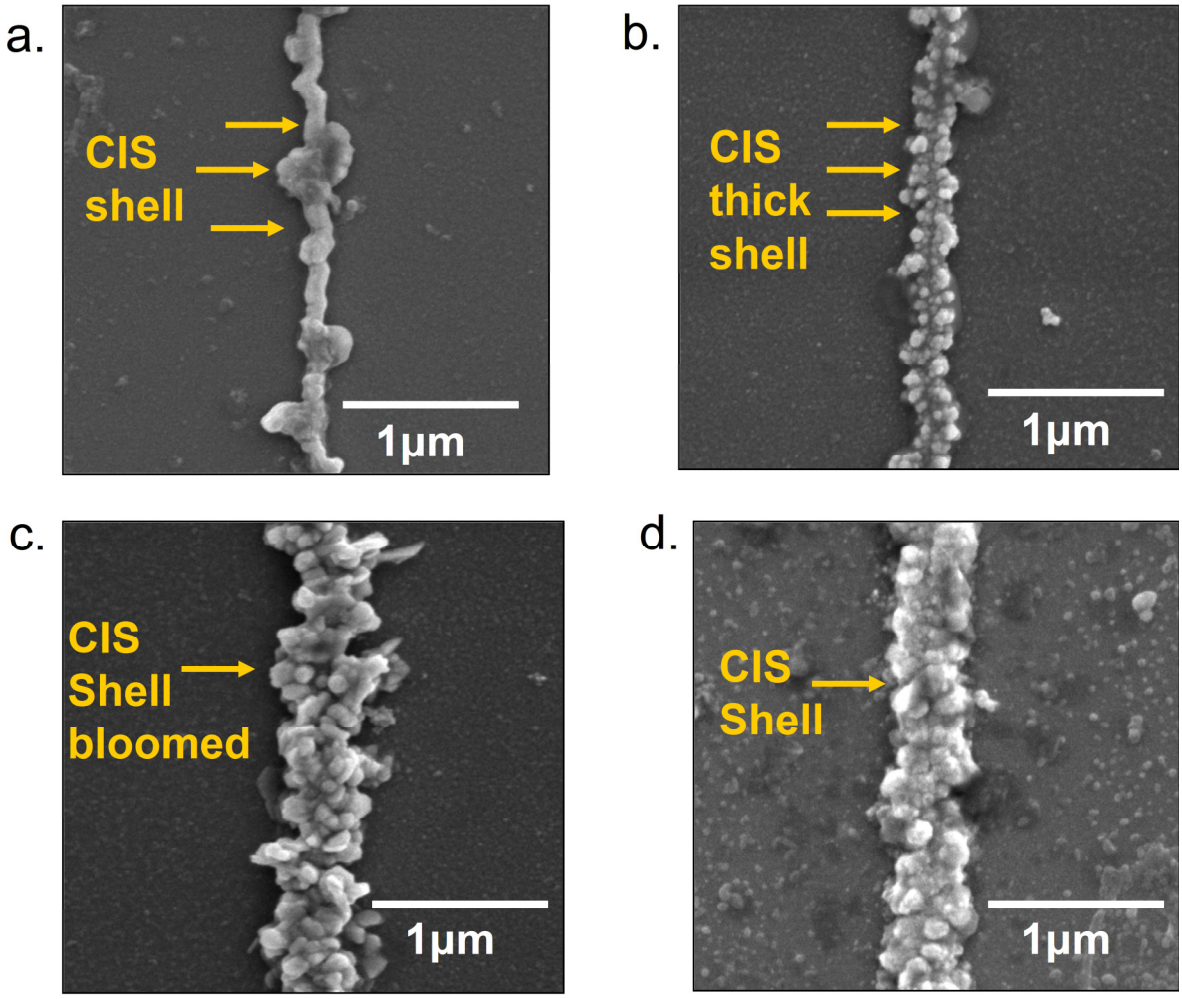

Figure 3.9 a) SEM image of very thin CIS shell on top of Au NW. b) Growth of CIS grains after electrodepositing for 500s. c) Very thick and bloomed CIS shell after electrodepositing for 800s. d) Annealed Au/CIS coaxial NW at 250 ℃ for 4 hrs in atmospheric pressure.

Figure 3.9a shows the growth process of CIS shell on top of Au NW. As the electrodeposition time increases the shell gets thicker and the growth can be seen in terms of grains growing on top of thick CIS shell (figure 3.9 b and c). Obtained Au/CIS coaxial NWs were also annealed at 380℃ for 4 hours in atmospheric pressure to make shell smoother as shown in figure 3.9 d.

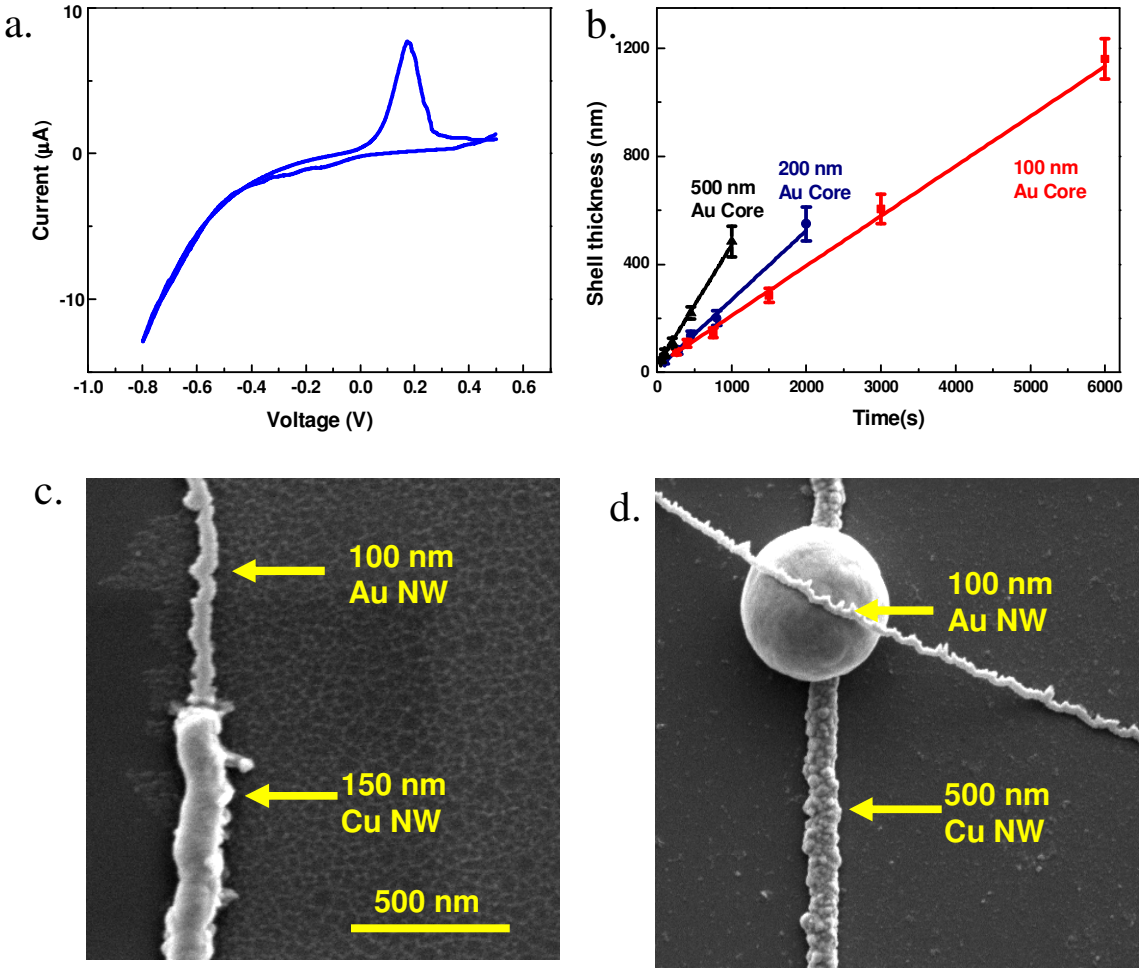

Figure 3.10. a) CV of the Cu electrodeposition solution. b) Calibration curves relating the CIS shell thickness to electrodeposition time and gold NW width. c) SEM image showing a 100 nm gold NW with a 150 nm Cu shell. d) SEM image showing a 100 nm gold NW with a 500 nm Cu shell.

Figure 3.10a shows a CV of the Cu electrodeposition solution with a gold NW array working electrode. The broad peak between +0.3 V and -0.4 V vs. Ag/AgCl corresponds to the deposition of copper while the oxidation that occurs near 0.15 V vs. Ag/AgCl. The SEM image in figure 3.10b shows a single 100 nm wide gold NW that has been held at a potential of -0.3 V

vs. Ag/AgCl for 500 seconds in the Cu deposition solution. The gold NW, which can be seen in the top portion of the image, has been coated with approximately 150 nm of copper. As with the Cu deposition above, the width of this coating depends on both the electrodeposition time and the width of the gold NW, as the calibration curve in figure 3.10c shows. The SEM image in figure 3.10 d shows a single 100 nm wide gold NW sitting on top of a unknown particle. The gold NW, which can be seen in the top portion of the image, has been coated with approximately 500 nm of copper.

To understand the structural characteristics of the semiconductor shell on top of gold NWs, we have performed transmission electron microscopy (TEM), selected area electron diffraction (SAED), and powder X-ray diffraction (XRD) studies on the Au/CIS core/shell NWs. Figures 3.11a and 3.11b, shows the TEM image and SAED of Au/CIS coaxial NW respectively. As it is evident from the TEM image, the center of the NW is much denser than the edges, corresponding to a gold core with a semiconductor shell, with a high contrast in gray scale between the core and the shell indicating that the gold-semiconductor boundary is pretty sharp. Also, the grains that make up the shell are much larger than the Au core, with the grain boundaries primarily along the axial direction. Furthermore, SAED micrographs for Au/CIS (fig. 3.11b) coaxial NWs confirm the presence of Au core and semiconductor shell. In both the SAED micrographs, the electron diffraction from the gold core shows as rings, corresponding to the nanocrystalline nature of the gold NW, while the electron diffraction from the shell shows up as individual spots, indicating fewer, larger grains.

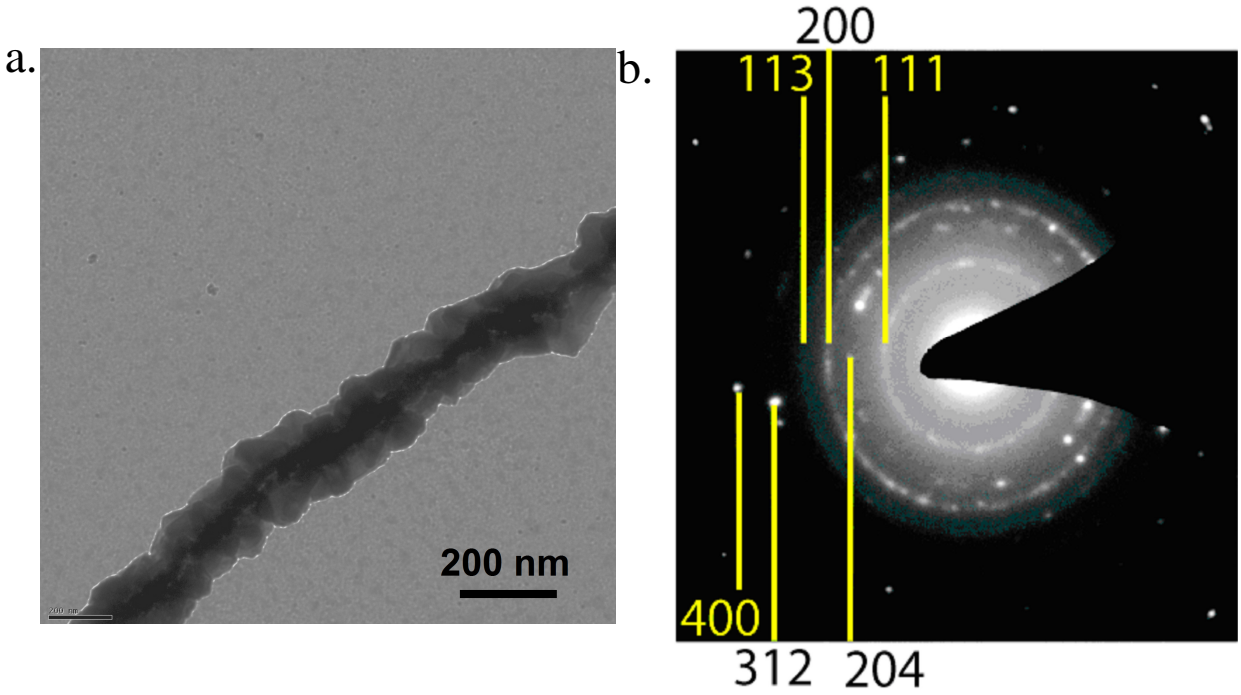

Figure 3.11. a) TEM image of a Au/CIS coaxial NW. b) SAED image of a Au/CIS coaxial NW with the 111, 200, and 113 peaks of gold and the 204, 312, and 400 peaks of CIS labeled.

XRD spectra on arrays of Au/CIS coaxial NWs (fig. 3.12) show individual peaks from Au core and semiconductor shells. The peaks shown in the

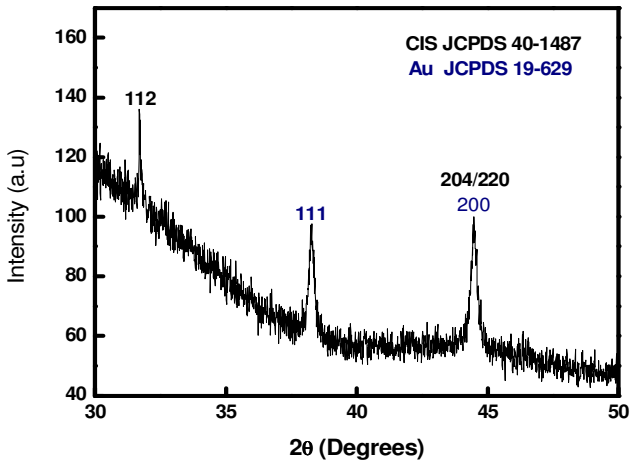

Figure 3.12 XRD spectra of a Au/CIS coaxial gold NW array with the 111 and 200 peaks of gold and the 112 and 220 peaks of CIS labeled.

XRD spectra correspond to only gold (JCPDS 19-629) and chalcopyrite tetragonal CIS (JCPDS 40-1487).

To understand the optical property of these coaxial NWs, we have measured UV-Vis absorption spectroscopy of the NW arrays. We have performed a comparative study of optical absorbance of the NW arrays with core/shell structure, just core and bare clean glass substrates over a wavelength of 400 to 800 nm as shown in fig. 3.13. In fig. 3.13 the optical absorbance of the curve labeled "Glass" corresponds to a clean glass slide and serves as a reference. The curve labeled "Au NW" in the same figure corresponds to an array of gold NWs with widths of 100 nm and heights of 40 nm running the length of the sample and separated by 12 μm. The noticeable increase in the absorbance over the glass is due to both absorption and light scattering by the gold NWs and the residual nickel on glass surface . Compared to Au NW arrays, a considerable increase in absorbance has been observed by electrodepositing approximately 250 nm of CIS (Au/CIS curve) onto 100 x 40 nm Au NWs, which can be attributed to light absorption by the semiconductor shells.

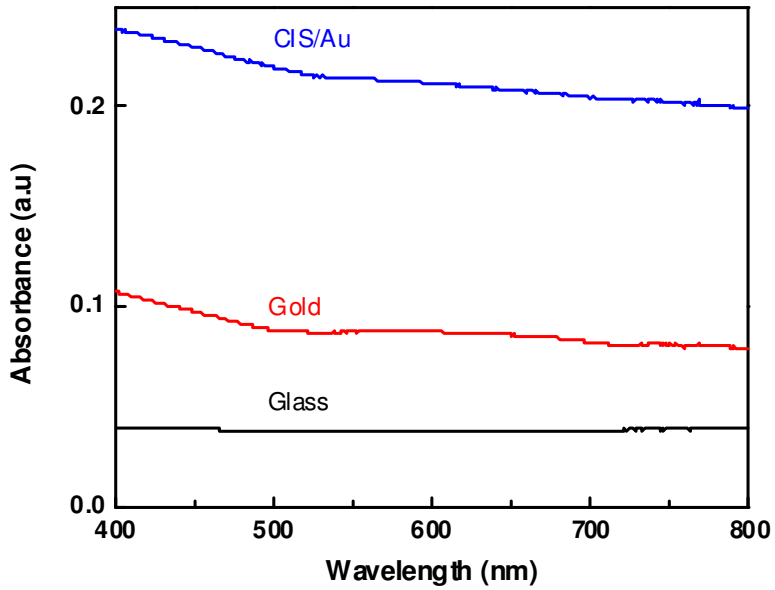

Figure 3.13. UV-Vis extinction spectroscopy of a glass substrate (red), an array of 40 x 100 nm gold NWs (red), an array of 40 x 100 nm gold NWs coated with 250 nm of PbSe (pink), and an array of 40 x 100 nm gold NWs coated with 250 nm of CIS (blue).

Light IV measurements were performed on Au/CIS NWs to test the light absorbtion by the semiconductor shell on top of Au core. The electrical contacts were made using conductive silver paste and these contacts were 500 µm apart. There were about 400 NWs on each samples tested for IV characteristics. The sample was cooled down to room temperature using peltier cooler. Front side of the NW sample was held normally to the incident light. Fig 3.14 shows current-voltage (IV) curves over a potential range of -2 V to +2 V of an array of CIS-coated gold NWs in the dark (black curve) and exposed to white light from a solar simulator (red curve) with an AM 1.5 filter, the sample shows an increase in conductivity

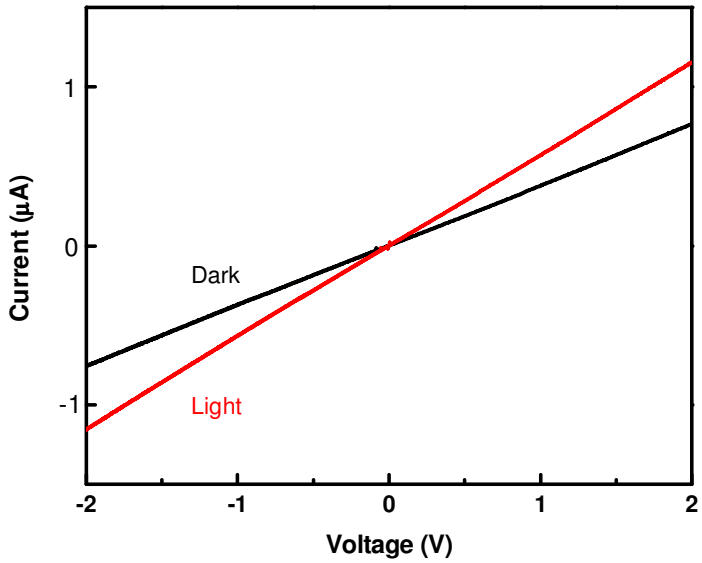

Figure 3.14 LIV and DIV curves of an array of 40 X 100 nm gold NWs coated with 250 nm of CIS shell width

when illuminated and fairly ohmic behaviour, indicating good electrical contact with the gold core.

The increase in the conductivity is mainly due to heating of the sample, rather than the just the direct creation of excitons by photon absorption. This can be seen in Figure 3.15a, which shows the current through a CIS-coated gold NW array constantly biased at at +1 V as a function of time. After turning on the light at approximately 20 s, a slow increase in the current over approximately 10 s has been observed, which is too slow to be an optical effect and is instead attributed to an increase in sample temperature due to plasmon-induced heating of the gold core, but also due to other factors, including Joule heating and light absorption by the substrate. The current dependence on temperature of the CIS coated gold NWs is further analyzed in Figure 3.15b, where IV curves on an array of CIS-coated gold NWs were measured at 15 (black curve), 28 (blue curve), 40 (violet curve), 50 (orange curve) and 60 ^{o}C (green curve). These curves show an increase in conductivity with increasing temperature, consistent with

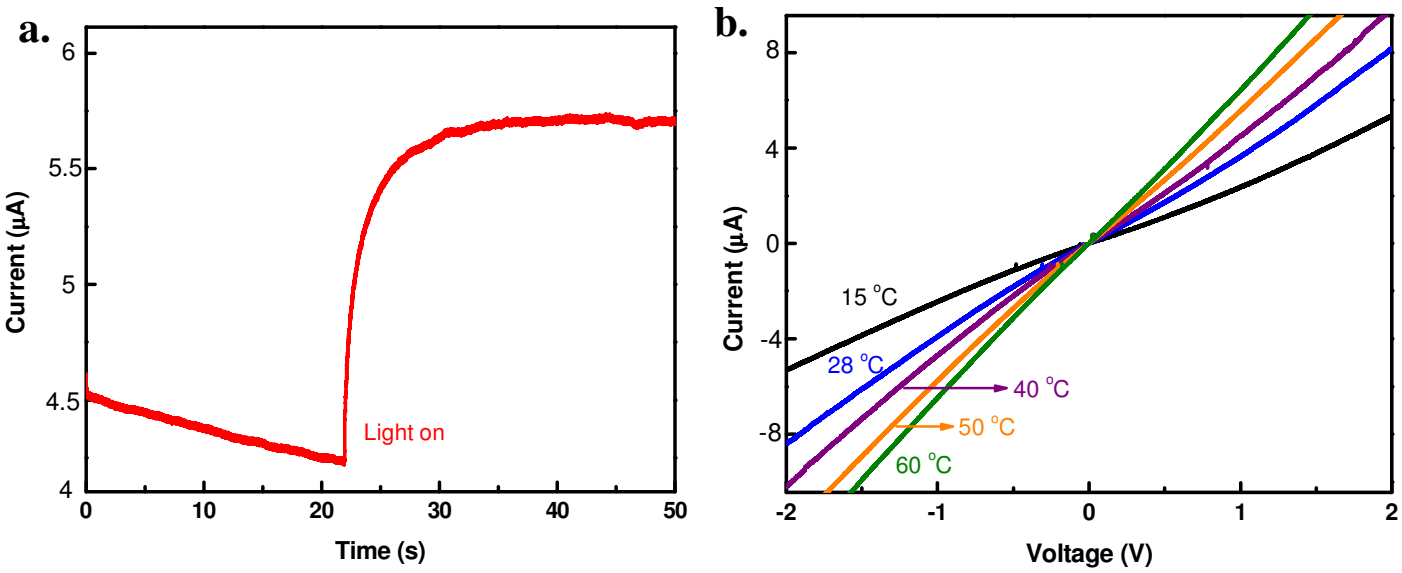

Figure 3.15. (a) The current through an array of 40 X 100 nm gold NWs coated with 250 nm of CIS before and after light exposure. (b) IV curves on an array of 40 X 100 nm gold NWscoated with 250 nm of CIS at temperatures of 15 (black curve), 28 (blue curve), 40 (violet curve), 50 (orange curve) and 60 (green curve) ^{o}C.

electronic conduction through a semiconductor The study of temperature dependent DIV curves gives us an estimate of temperature increase of approximately 10 ^{o}C when the samples are illuminated with the white light from a solar simulator, which is consistent with other reported experiments on plasmon heating [110, 111]. Previous measurements on gold NWs prepared via LPNE have shown a decrease in conductivity with increasing temperature, indicating that the semiconductor shell controls the electrical conductivity of the core/shell NWs [112].

When Au/CIS coaxial NW is irradiated with photons of sub-band gap energy, it is possible to excite carriers from the metal into the semiconductor.

Light transport measurements were performed at incident chopped illumination to understand the pulsed response of photocurrent of Au/CIS coaxial NWs as shown. A comparative study of photoresponse of Au/CIS coaxial NWs and a commercial photodiode was performed by edge

Trigger measurements as shown in Fig. 3.16(a). It shows that photoresponse of Au/CIS NWs are faster then photodiode.

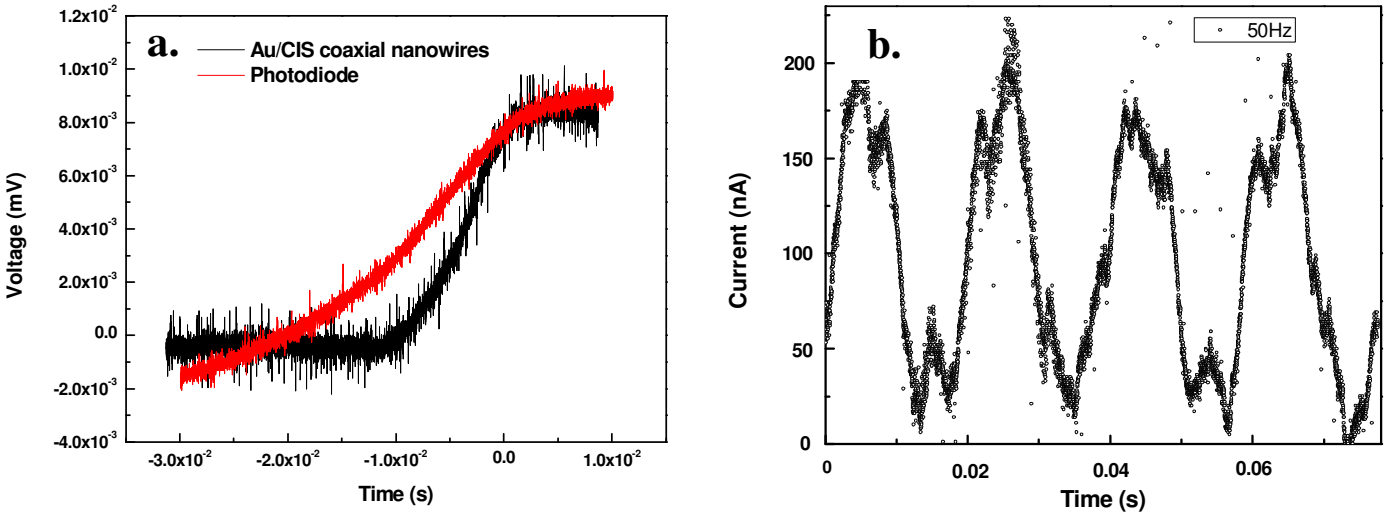

Figure 3.16. a) Photoresponse of Au/CIS coaxial NWs and commercial photodiode (b) On-off behavior of photocurrent of Au/CIS NW sample at 50 Hz

On-off behavior of the photocurrent generated by Au/CIS NWs were measured at 50Hz as shown in Fig. 3.16b. It shows a change of 0 to 200 nA of photocurrent at 1 V of biasing voltage. The higher frequency response were also measured but the photocurrent seemed to decrease after 500Hz oNWards.

The photoconductivity of the CIS-coated gold NW arrays were also measured as a function of incident wavelength in Fig. 3.17. The photocurrent signal from the NWs was amplified using a current preamplifier and the converted output voltage from current preamplifier was connected to a Lock-in amplifier to remove the ripple factor.

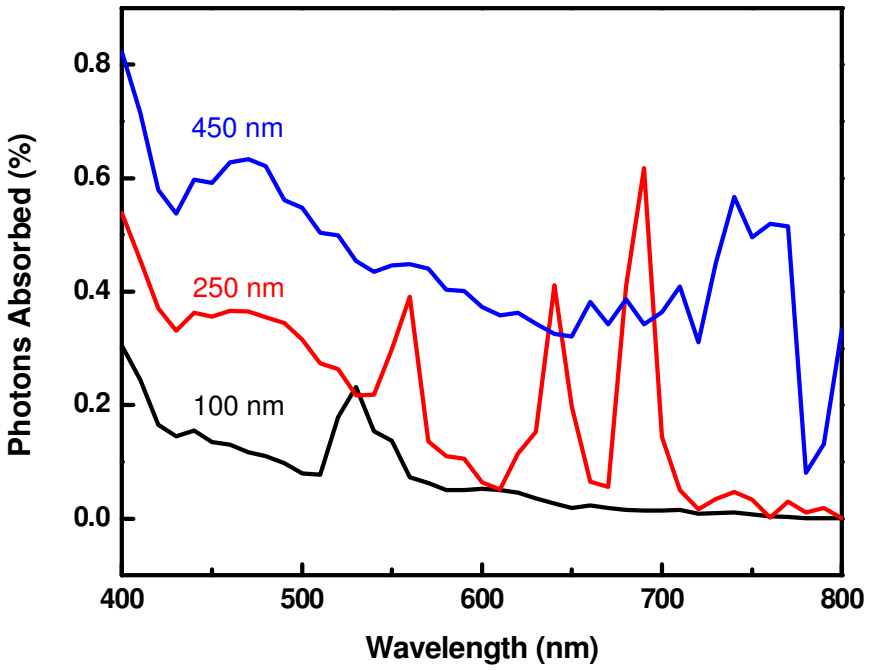

Figure 3.17. Comparison of the absorption efficiency of incident photons absorbed by an array of 40 X 100 nm gold NWs coated with 100 nm of CIS (black), an array of 40 X 100 nm gold NWs coated with 250 nm of CIS (red), and an array of 40 X 100 nm gold NWs coated with 450 nm of CIS (blue).

By comparing the current through the NW array with the incident photon flux, and again assuming unit conversion efficiency, we find the percentage of photons absorbed by the sample. We see narrow regions of enhanced absorption in both 100 nm and 250 nm wide CIS shell width, which red shifts as the NWs increase in size, as can be seen in Fig. 3.17. As a result of the regions of enhanced absorption, we find that, while the 450 nm wide NWs absorb more light, the 250 nm wide NWs are more efficient at absorbing light than either the 100 or the 450 nm wide NWs, as summarized in Table 1. The explanation for the increase in absorption efficiency is due to the presence of leaky-mode resonances, first predicted and then observed by Cao et al. in single-crystal NWs [113, 114].

CIS Shell width (nm)	Light absorbed by sample (%)	Active area (%)	Light absorbed by NWs
100	0.1	1.7	6
250	0.29	2.9	9.9
450	0.45	4.6	9

Table 3.1. Average Photon-to-Electron Conversion Efficiency for Different CIS widths

The findings of our study shows that it is possible to generate LMR inside nanocrystalline coaxial NWs to spectrally tune and enhance fundamental absorption properties. This work also shows that light absorption in NW devices can be tuned through control over the size of the nanostructure which is quite similar to what Cao et al. has shown in his work. The concept of using LMRs of semiconductor structures can be applied directly to engineer absorption spectra for NW-based solar cells and photodetectors.

Chapter 4

Core/Shell Nanowire Solar Cell prepared by Lithographically Patterned Nanowire Electrodeposition

4.1 Motivation

Coaxial, Metal/semiconductor hetero junction semiconductor nanowiress are the best candidates for the fabrication of next generation of solar cell [115]. Metal/Semiconductor hetero junction combines the plasmonic properties [26] of metal core and the cavity effect of the semiconductor shell [113]. Currently, two important compound semiconductor materials for use in solar cells are $CuInSe_2$ (CIS) and CdS. An advantage associated with CIS in solar cells is that CIS related materials have the highest reported power conversion efficiency (~19.5%) among all the thin-film solar cell technologies and can be easily doped into a p-type semiconductor. Similarly, CdS, a wide bandgap II–VI semiconductor (2.4 eV), is one of the best known materials for n-type doping.

CIS is a direct-band gap chalcopyrite semiconductor with high optical absorption coefficients ($>10^5$ cm^{-1}) and is thus used as a photon-absorber in thin-film solar cells. CIS is commonly paired with CdS to form the p-n heterojunction that separates the photo-generated electron-hole pairs. The pn junction is formed between the p-type CIS absorber layer and the n-type CdS and ZnO layers as shown in Fig. 4.1 [116], which causes bending of the valence and conduction bands. The CIS layer divides into a majority charge carrier depleted space charge region (SCR)

and a quasi-neutral region (QNR). Incoming light with higher energy than the CIS bandgap is mostly absorbed within the absorber layer, where it creates electron-hole pairs that are spatially separated by the internal electric field at the pn junction.

A successful fabrication of a precise interface between CIS and CdS is of key importance to the performance of the solar cell device. CdS finds extensive applications in nonlinear optical materials, light-emitting diodes, solar cells,

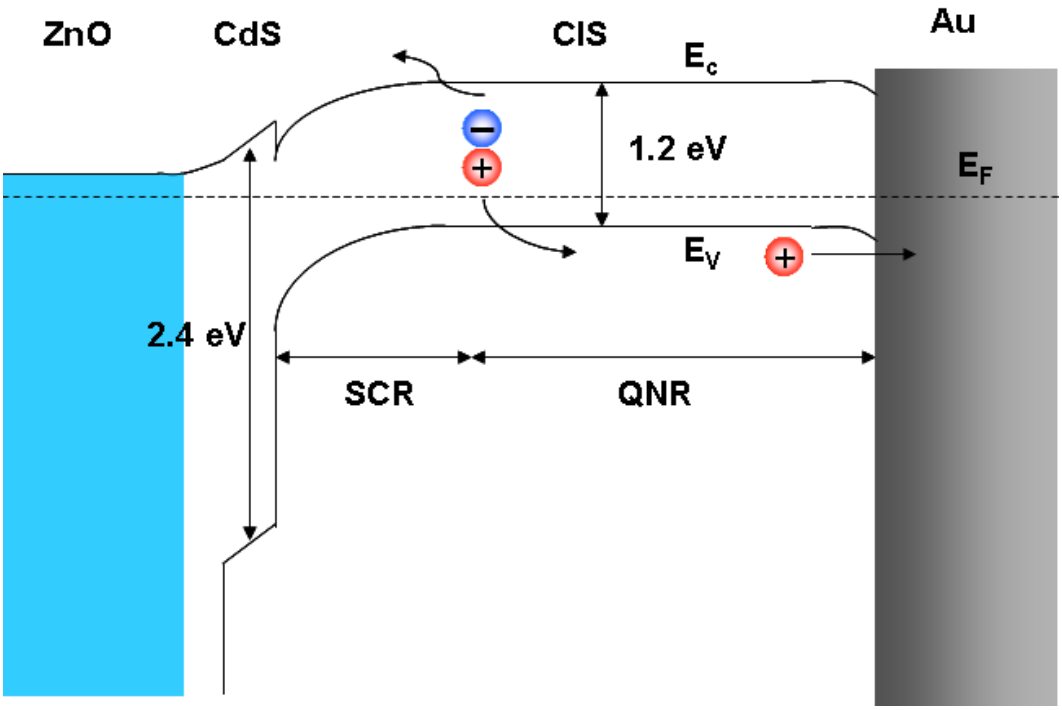

Figure 4.1. Band diagram of Au/CIS/CdS/ZnO Solar Cell

electronic and optoelectronic devices property [116]. CdS nanowiress have been synthesized by several techniques including template-assisted electrochemical synthesis [117], laser ablation [118], vapor–liquid–solid [119], colloidal micelle [120], solvo-thermal methods [121], etc. Because of these inherent advantages, CIS/CdS (p-n) coaxial heterostructure provide the strong platform for fabricating high-efficiency solar cell.

Traditionally, electrochemical techniques have been used to grow semiconductor thin films on conductive surfaces. Because electrochemical techniques are inexpensive, operate at ambient temperatures and pressure, and provide film thickness control. In our case, CdS nanowires were electrodeposited (Fig. 4.2) on top of a Au/CIS core-shell nanowires prepared by a novel method of lithographically patterned nanowire Electrodeposition method (LPNE). The major advantage of this technique is the capability that allows for spatially controlled growth of nanowires on pre-selected sites. This method also combines the fact that Gold core nanowire helps to enhance the absorption of white light by the Semiconductor shell by scattering the light through sharp edges of the Gold core. Core/Shell structure helps to sweep out the electron-hole pairs as soon as they are created. Therefore, our approach towards making cheap and efficient solar cell combines plasmonics and cavity effects due to semiconductor shells.

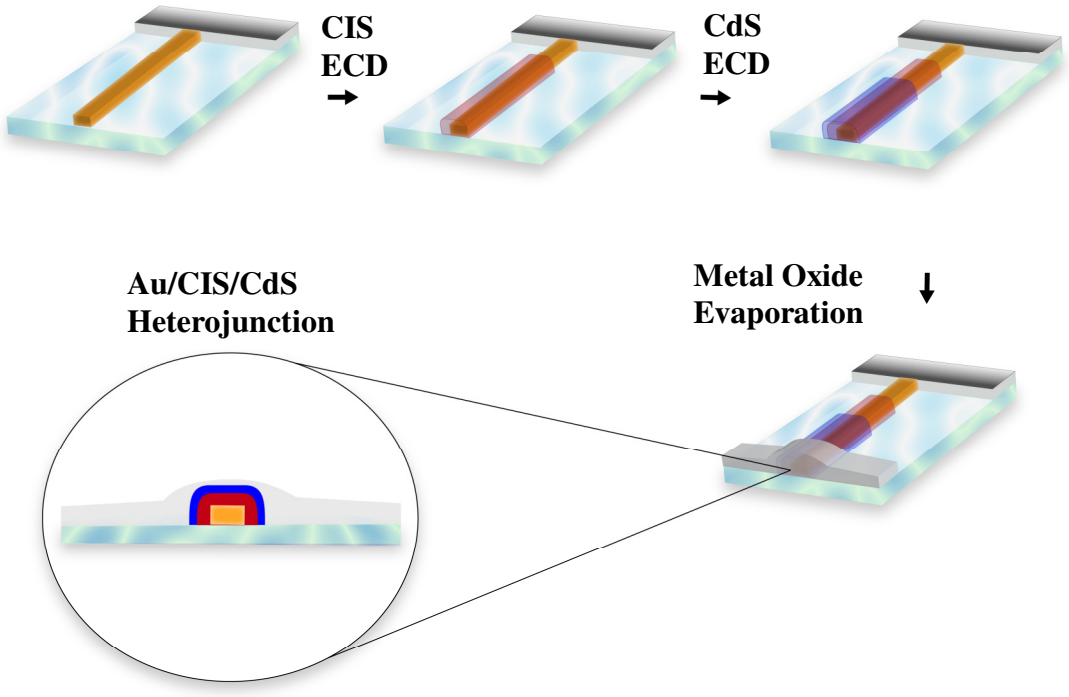

Figure 4.2. Schematics of Core/Shell NW solar cell fabrication

4.2 Experimental Details

We synthesized copper-indium-diselenide (CIS) nanowires on Au core nanowires by a constant potential method following procedure used by Phok *et. al*. In this method, CIS electrodeposition on Au core nanowire is achieved from a deposition solution containing 1.5 mM $CuSO_4$ (Sigma Aldrich, Purity 99.99% metal basis), 2 mM $InSO_4$ (Sigma Aldrich, Purity 99.99% trace metal basis), and 1 mM SeO_2 (Sigma Aldrich, Purity 99.999%) in NANOPure water (resistivity = 18.0 $M\Omega$ cm), with the final solution pH adjusted to 2.8 by the drop-wise addition of 1 M H_2SO_4 (Sigma Aldrich, Reagent grade). Co-deposition of Cu, In and Se is ensured between a potential range of -0.55 V to -0.6 V versus Ag/AgCl in a three-electrode cell at RT conditions without excess component wise deposition of Cu, In, or Se in shell NW.

For obtaining Au/CIS nanowires the steps involved are the same as described above. For depositing CdS over previous Au/CIS nanowires heterostructure (Fig. 2, step 2), a solution containing 10 mM $Na_2S_2O_3$ (Sigma Aldrich, Purity 99.99% metal basis), 2.5 mM $CdSO_4$ (Sigma Aldrich, Purity 99.99% metal basis) was used. The pH of this solution was adjusted to 4.0 by dropwise addition of 0.8 M HNO_3. Co-deposition of Cd and S (CdS shell) was ensured between a potential range of -0.65 V to -0.9 V versus Ag/AgCl in a three-electrode cell at RT conditions for 700 to 900 seconds.

Quantum Efficiency and transport Measurements:

To characterize the dark current response of the device under test (DUT), I-V measurements were done using Princeton Applied Research (PARSTAT 2273) potentiostat/galvanostat. Photocurrent measurements were performed using commercially available Oriel (Newport Inc.) full spectrum 96000 solar simulator with white light (Xe lamp) source in AM1.5G condition. External quantum efficiency of the cell was measured by chopping the incident light using a

mechanical chopper at different frequencies (50-400 Hz) as shown in Fig. 4.3. The photocurrent was amplified using a Keithley 428 PROG current amplifier in the path and signals were fed to a Lockin amplifier.

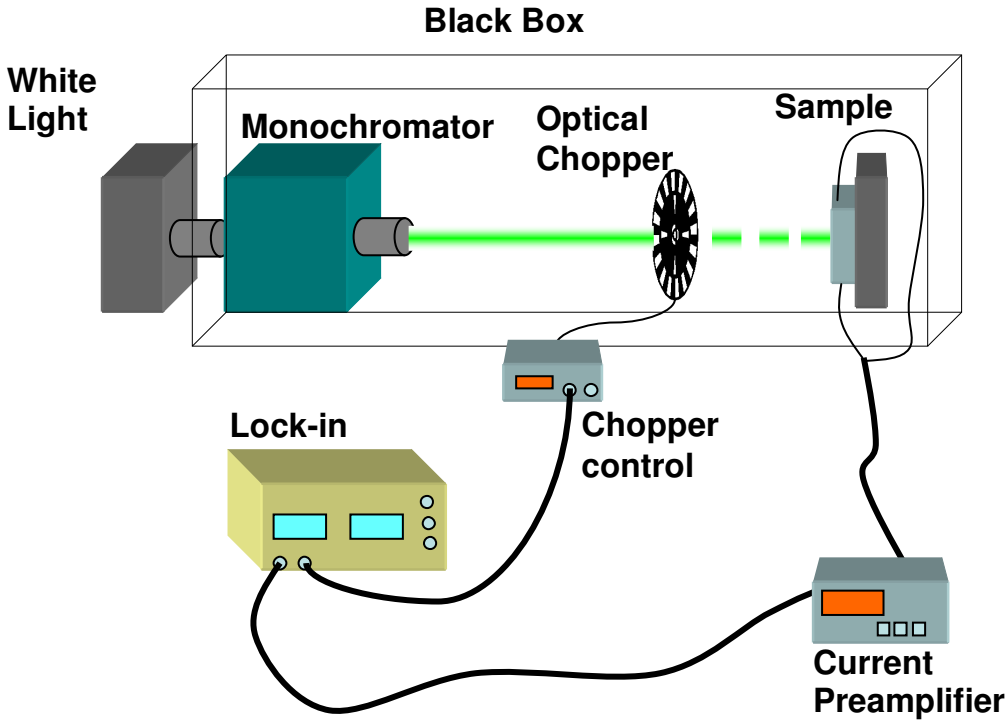

Figure 4.3. Experimental setup to measure external quantum efficiency of the Solar Cell

4.3 Results and Discussions

Figure 4.4 shows a cyclic voltamogram (CV) of the CdS electrodeposition solution with a Au/CIS array working electrode. The broad peak between -0.5 V and -8.0 V vs. Ag/AgCl corresponds to the co-deposition of Cadmium and Sulphur, while the reduction that occurs below -1.0 V vs. Ag/AgCl is due to hydrogen formation.

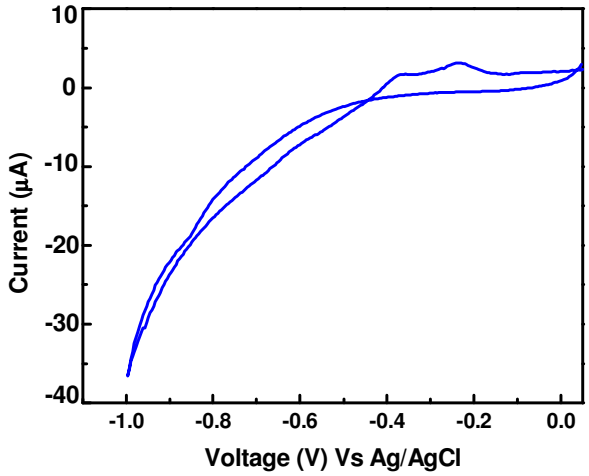

Figure 4.4. CV of the CdS electrodeposition solution

The scanning electron microscopy (SEM) image in figure 4.5 shows a single 100 nm wide gold nanowire coated with 200 nm CIS shell that has been held at a potential of -0.6 V vs. Ag/AgCl for 7000 seconds in the CdS deposition solution.

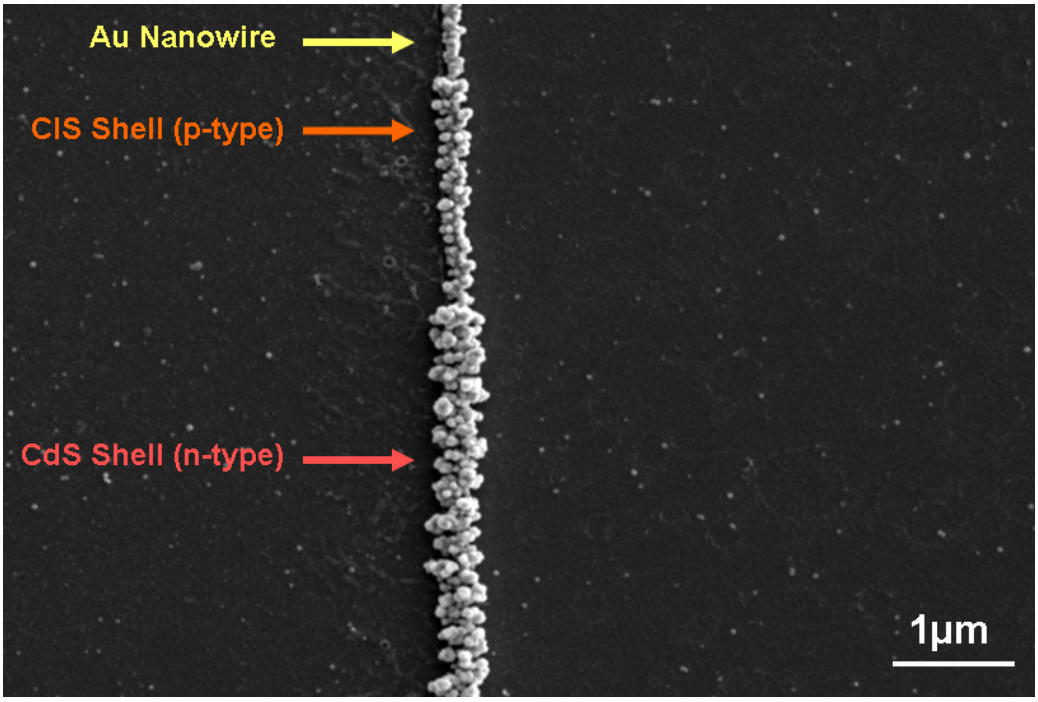

Figure 4.5. SEM image showing a 100 nm gold NW core and 200 nm CIS shell with a 300 nm CdS shell coated on top

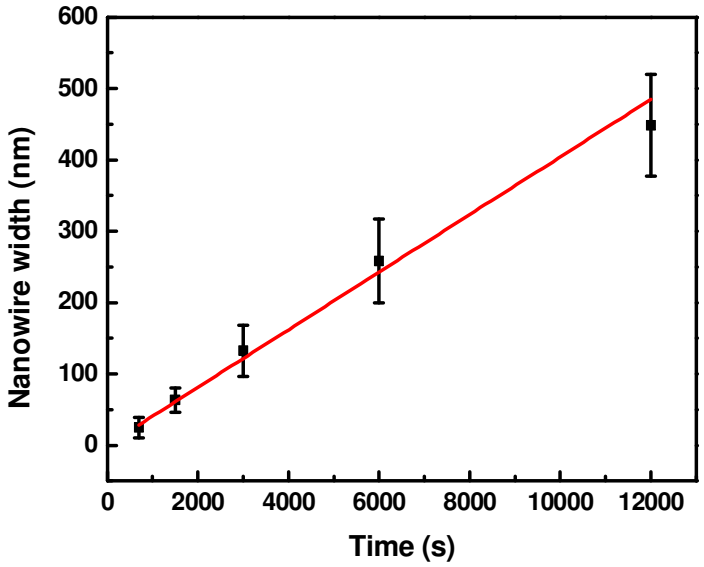

Figure 4.6. Calibration curve relating the CdS shell thickness to electrodeposition time.

The Au/CIS nanowire, which can be seen in the top portion of the SEM micrograph, has been coated with 300 nm of CdS shell. The width of this shell depends on both the electrodeposition time as shown in the calibration curve in figure 4.6.

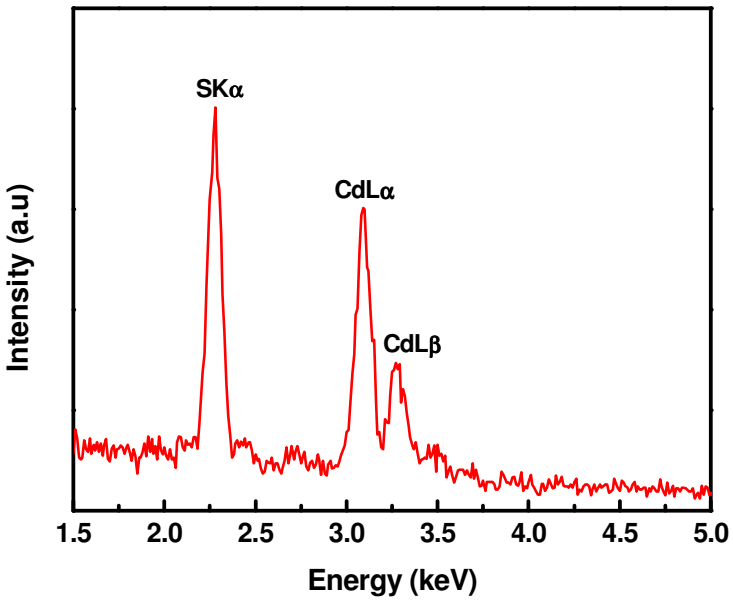

Figure 4.7. EDAX spectrum of CdS NW shell on Au/CIS coaxial NW

The chemical composition of the nanowires was determined by X-ray energy dispersion analysis (EDAX). The EDAX spectrum shown in Fig. 4.7 reveals that the nanowires are composed of Cd and S. Quantitative analysis result indicates that the atomic composition is 51.4% S and 48.6% Cd, which is very close to 1:1 stoichiometry.

The XRD spectrum of CdS shell deposited on Au/CIS coaxial nanowire is shown in Fig. 4.8, where the diffraction peaks could be assigned to peaks of CdS shell without elemental Cd and S. These diffraction peaks of CdS were observed close to 2θ = 43.9, 52.09 corresponding to the (220) and (113) (JCPDS 10-454) diffraction planes of cubic CdS crystalline, respectively

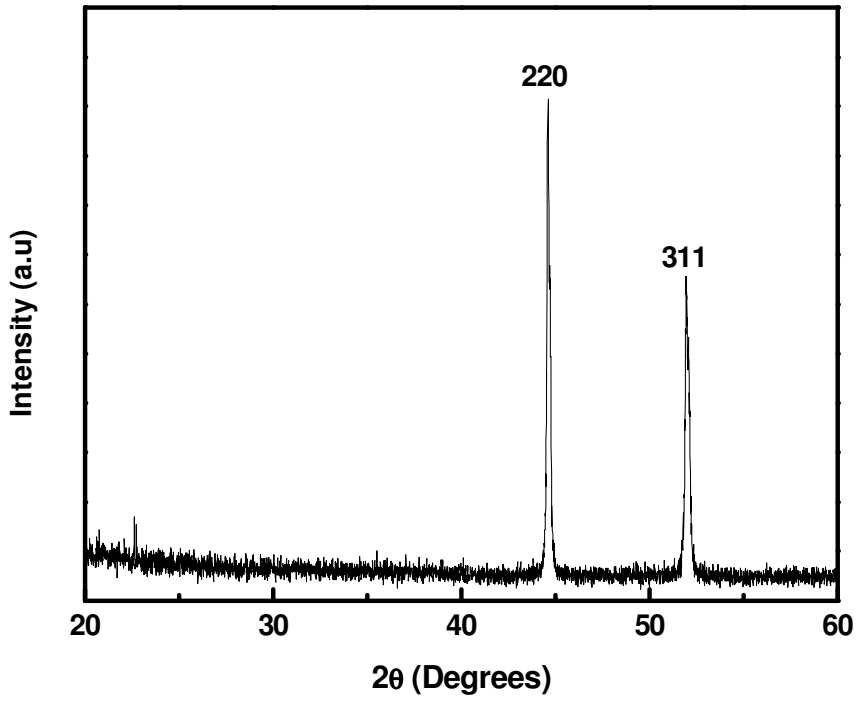

Figure 4.8. Powder XRD pattern of the CdS NWs shell

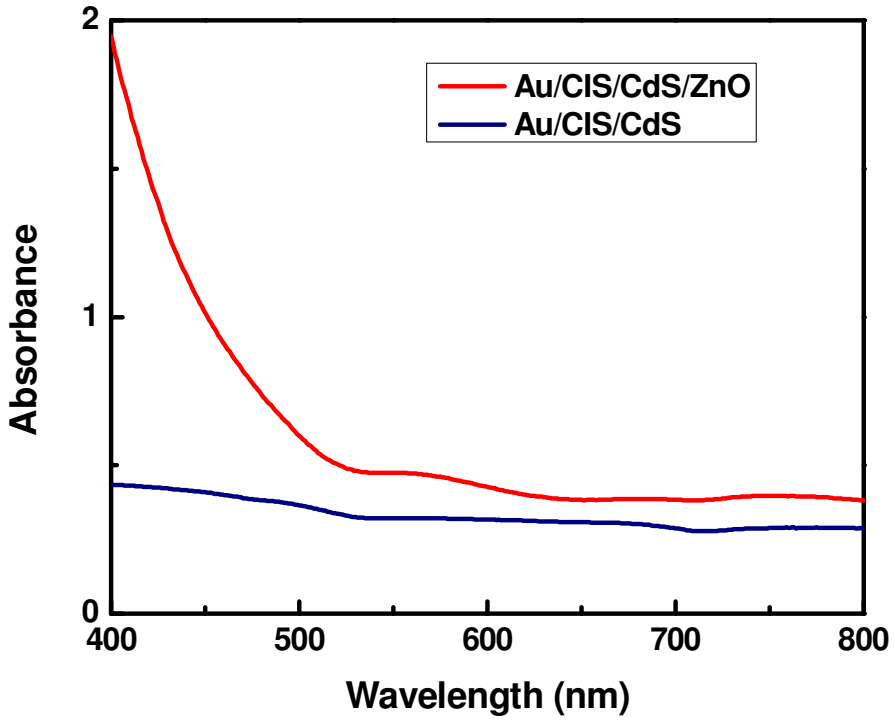

Figure 4.9. UV-VIS Absorption spectra of samples with Au/CIS/CdS (blue curve) and Au/CIS/CdS/ZnO (red curve) nanowires

Optical absorption properties were studied by UV-VIS absorption spectroscopy measurement of the nanowire solar cell as shown in Fig.4.9. The solar cell sample coated with ZnO thin films shows enhanced absorption of light compared to the cell which does not have the ZnO coating on top because ZnO acts as a window layer [122] and lets the solar cell absorb sunlight efficiently.

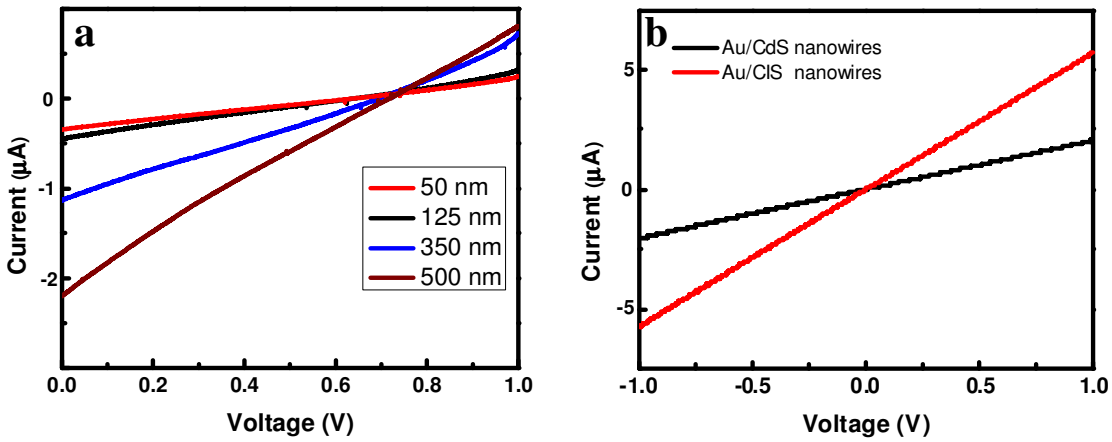

Figure 4.10 Current-Voltage (IV) characteristics measured at AM1.5 of (a) Au/CIS/CdS/SnO_2/Al nanowire solar cell where Aluminum (Al) acts as a metal contact and also back reflector. The white light was shined through the backside of the glass substrate (b) Au/CIS/Al and Au/CdS/Al nanowires

Fig. 4.10a shows the IV characteristics of Au/CIS/CdS/ZnO/Al core/shell nanowire solar cell of different CIS shell widths of 50, 125, 350 and 500 nm respectively. The solar sell has on average about 400 nanowires on a 1 $inch^2$ glass substrate. For all the samples, gold core and CdS shell width of 100 nm and 25 nm respectively were kept constant. The measured cells had an open circuit voltage (V_{oc}) of ~0.68 V and short circuit current (I_{sc}) in the range of 330 nA to 2.2 μA depending on the CIS shell width. The efficiency of the solar cell with CIS shell width of 200 nm was calculated considering 1 $inch^2$ area of the substrate. The actual efficiency of the cell would be much higher then 1% if we consider only the active area of the sample having nanowires. The Fill Factor (FF) of the cell was measured to be 24.7%. Cell verification tests were performed by removing either CIS or CdS layers and corresponding IV characteristics as shown in fig. 4.10b proves that there was no V_{oc} observed in either case. Only short circuit current was

observed in both the cases. That also shows that a pn junction solar cell will not work if either p-type CIS layer or n-type CdS layer is absent in the device.

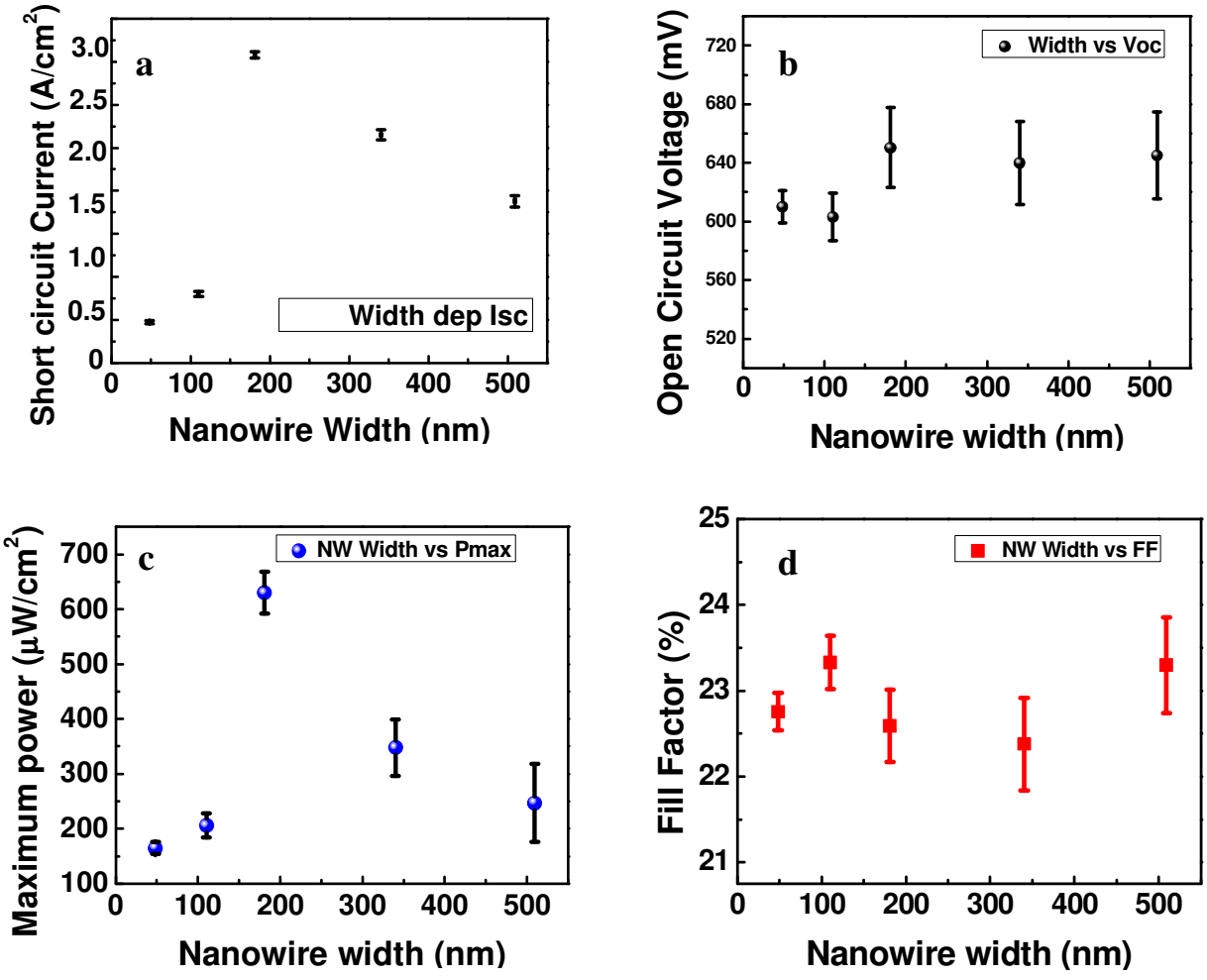

Figure 4.11. CIS Shell Width dependent variation of (a) Short circuit current (I_{sc}) density (mA/cm^2) (b) Open circuit voltage (V_{oc}) (c) Maximum power (P_{max}) density (μW/cm^2)(d) Fill Factor (FF %). To study the solar cell parameters, four samples were prepared for corresponding CIS shell width

A systematic study of the CIS width dependent variation of Solar Cell parameters was performed as shown in Fig. 4.11. Fig 4.11(a) shows that with the increase in CIS shell width, the short circuit current density in mA/cm^2 peaks at 180 nm CIS shell width and start falling down

afterwards. For calculation of current density, the length of the active area was considered to be 0.7 inches. There was no trend observed in Open circuit voltage with change in CIS shell width as shown in Fig. 4.11 (b). Maximum power density in $\mu W/cm^2$ of the Solar Cell increases with the increase in CIS shell width and peaks at 180 nm CIS shell width as shown in Fig. 4.11 (c). Fig. 11 (d) shows that there was no trend observed in Fill Factor (%) with respect to CIS shell width.

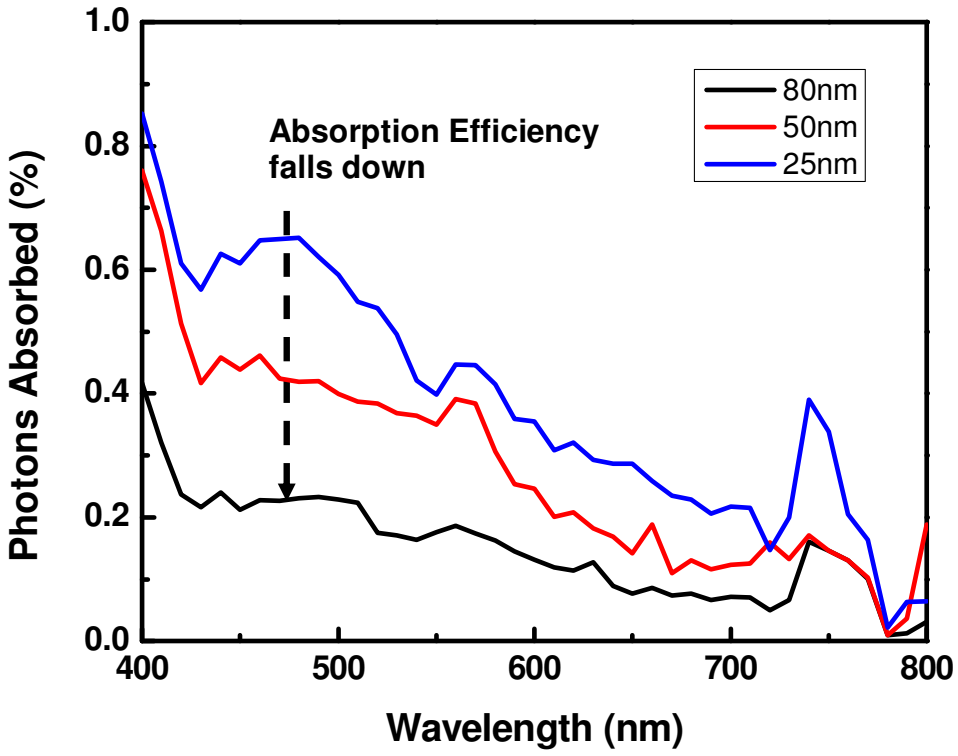

Figure 4.12. CdS Shell width dependent variation of Absorption efficiency of Au/CIS/CdS Solar Cell

Incident wavelength dependent Absorption efficiency [123] of the cell was performed and it shows that with the increase in CdS shell width the Absorption efficiency of the cell fall down as shown in Fig. 4.12. The fall in Absorption efficiency with respect to increase in CdS shell width is because CdS is a wide bandgap material and if it is optically thick then it will be tough to

absorb the white light. Thick CdS shell also reduces the efficient separation of electrons from holes [124].

4.4 Future Work

Solar Cell on Flexible substrate

We have successfully fabricated the nanowires on Plastics. We want to continue this process by fabricating the whole Solar Cells on Plastic/Paper substrates.

Single variable tests (SVTs) to obtain the maximum efficiency of the cell

a. CIS deposition potential dependent study of Solar Cell parameters

b. CdS width dependent study of Solar Cell parameters

c. Gold core width dependent study of Solar Cell parameters

Mott-Schotky measurement on Au/CIS nanowires

Mott-Schotky measurement helps to find the buildup potential and carrier concentration. A systematic study needs to done to find out the carrier concentration in CIS shell at different deposition potential.

Experiments with different core metals

Optical characterization

a. Photoluminescence study of nanowires

b. Time resolved Photoluminescence to understand the charge dynamics

Bibliography

[1] M. A. Green, Prog. Photovolt: Res. Appl. ; 17:183, 2009.

[2] J. Nelayah, M. Kociak, O. Stéphan, F. J. G. Abajo, M. Tence, L. Henrard, D. Taverna, I. P. Santos, L. M. L. Marzán and C. Colliex, Nature Physics, 3:348, 2007

[3] P. Andrew and Barnes, *Science,* 306**:**1002, 2004.

[4] H. Mertens, J. S. Biteen, H. A. Atwater, and A. Polman, *Nano Letters,* 6**:**2622, 2006.

[5] S. Kuhn, U. Hakanson, L. Rogobete, and V. Sandoghdar,, *Phys. Rev. Lett.* 97**:**017402, 2006.

[6] M. I. Stockman, P*hys. Rev. Lett.* 93**:**137404, 2004.

[7] E. Verhagen, M. Spasenović, A. Polman, and L. Kuipers, *Phys. Rev. Lett.* 102**:**203904, 2008.

[8] E. Prodan, C. Radloff, N. J. Halas, and P. Nordlander, *Science* 302**:** 419, 2003.

[9] M. Quinten, A. Leitner, J. R. Krenn, and F. R. Aussenegg, *Opt. Lett.,* 23**:**1331, 1998.

[10] S. A. Maier, *Nature Mater.,* 2**:**229, 2003.

[11] A. F. Koenderink, and A. Polman, *Phys. Rev. B,*74**:** 033402, 2006.

[12] R. Zia, M. D. Selker, P. B. Catrysse, and M. L. Brongersma, *J. Opt. Soc. Am. A,* 21**:**2442, 2004.

[13] P. Muhlschlegel, H. J. Eisler, O. J. F. Martin, B. Hecht, and D. W. Pohl, S*cience,* 308:1607, 2005.

[14] H. Ditlbacher, J. R. Krenn, G. Schider, A. Leitner, and F. R. Aussenegg, *Appl. Phys. Lett.,* 81**:**1762, 2002.

[15] S. I. Bozhevolnyi, V. S. Volkov, E. Devaux, J. Y. Laluet, and T. W. Ebbesen, *Nature* 440**:**508, 2006.

[16] A. V. Krasavin, and N. I. Zheludev, *Appl. Phys. Lett.,* 84**:**1416, 2004.

[17] R. Colombelli, *Science,* 302:1374, 2003.

[18] M. T. Hill, *Nature Photon.*1**:**589–594, 2007.

[19] R. F. Oulton, *Nature,* 461**:**629, 2009.

[20] K. Okamoto, *Nature Mater.,* 3**:**601, 2004.

[21] J. B. Pendry, *Phys. Rev. Lett.,* 85**:**3966, 2000.

[22] R. A. Shelby, D. R. Smith and S. Schultz, *Science,* 292**:**77, 2001.

[23] S. Linden, *Science,* 306**:**1351, 2004.

[24] N. Fang, H. Lee, C. Sun, and X. Zhang, *Science,* 308**:**534, 2005.

[25] K. J. Vahala, *Nature,* 424, 839, 2003.

[26] H. A. Atwater and A. Polman, *Nature Materials,* 9:205, 2010.

[27] H. R. Stuart, and D. G. Hall, *Appl. Phys. Lett.,* 69**:**2327, 1996.

[28] H. R. Stuart, H. R. and D. G. Hall, *Appl. Phys. Lett.,* 73**:**3815, 1998.

[29] D. M. Schaadt, B. Feng and E. T. Yu, *Appl. Phys. Lett.,* 86**:**063106,2005.

[30] D. Derkacs, S. H. Lim, P. Matheu, W. Mar, and E. T. Yu, *Appl. Phys. Lett.,* 89**:**093103, 2006.

[31] P. Matheu, S. H. Lim, D. Derkacs, C. McPheeters, and E. T. Yu, *Appl. Phys. Lett.* 93**:**113108, 2008.

[32] S. Pillai, K. R. Catchpole, T. Trupke and M. A. Green, *J. Appl. Phys.,* 101**:** 093105, 2007.

[33] D. Derkacs, *Appl. Phys. Lett.,* 93**:**091107, 2008.

[34] K. Nakayama, K. Tanabe and H. A. Atwater, *Appl. Phys. Lett.* 93**:**121904,2008.

[35] K. R. Catchpole and A.Polman, *Appl. Phys. Lett.,* 93**:**191113, 2008.

[36] K. R. Catchpole and A. Polman, *Opt. Express,* 16**:**21793, 2008.

[37] G. Xu, M. Tazawa, P. Jin, S. Nakao and K. Yoshimura, *Appl. Phys. Lett.,* 82**:**3811, 2003.

[38] H. Mertens, J. Verhoeven, A. Polman and F. D. Tichelaar, *Appl. Phys. Lett.* 85**:**1317, 2004.

[39] F. J. Beck, A. Polman and K. R. Catchpole, *J. Appl. Phys.* 105**:**114310, 2009.

[40] L. Cao, J. S. White, J. S. Park, J. A. Schuller, B. M. Clemens and M. L. Brongersma, *Nat. Mater.,*8:643, 2009.

[41] L. Cao, P. Fan, A. P. Vasudev, J. S. White, Z. Yu, W. Cai, J. A. Schuller, S. Fan, and M. L. Brongersma, *Nano Lett.*, 10:439, 2010.

[42] B. M. Kayes, H. A. Atwater, and Nathan S. Lewis, J. Appl. Phys., 97: 114302, 2005

[43] M. Imaizumi, T. Ito, M. Yamaguchi, and K. Kaneko, J. Appl. Phys. 81:7635, 1997.

[44] S. Ghosh, W. H. Wang, F. M. Mendoza, R. C. Myers, X. Li., N. Samarth, A. C. Gossard, and D. D. Awschalom, *Nature materials*, 261, 2006.

[45] S. Strauf, K. Hennessy, M. T. Rakher,Y. S. Choi, A. Badolato, L. C. Andreani, E. L. Hu, P. M. Petroff, and D. Bouwmeester, *Phys. Rev. Lett*. 96:127404, 2006.

[46] M. Cai, O. Painter, and K. J. Vahala, *Phys. Rev. Lett*. 85:74, 2000.

[47] A. F. J. Levi, R. E. Slusher, S. L. McCall, S. J. Pearton, and W. S. Hobson, *Appl. Phys. Lett.*, 62:17,1993.

[48] D. K. Armani, T. J. Kippenberg, S. M. Spillane and K. J. Vahala, *Nature*, 421:925, 2003.

[49] J. M. Gérard, D. Barrier, J. Y. Marzin, R. Kuszelewicz, L. Manin, E. Costard, V. T. Mieg, and T. Rivera, *Appl. Phys. Lett*., 69:449, 1996.

[50] C. J. Hood, T. W. Lynn, A. C. Doherty, A. S. Parkins, and H. J. Kimble, *Science*, 287:1447, 2000

[51] J. M. G´erard, B. Sermage, B. Gayral, B. Legrand, E. Costard, and V. Thierry- Mieg., *Phys. Rev. Lett.*, 81: 1110, 1998.

[52] B. Gayral, J. M. G´erard, A. Lemaˆitre, C. Dupuis, L. Manin, and J. L. Pelouard, *Appl. Phys. Lett.*,75:1908, 1999.

[53] O. Painter, R. K. Lee, A. Yariv, A. Scherer, J. D. O'Brien, P. D. Dapkus, and I. Kim. *Science*, 284:1819, 1999.

[54] T. Yoshie, J. Vu˘ckovi´c, A. Scherer, H. Chen, and D. Deppe, *Appl. Phys. Lett.*, 79: 4289, 2001.

[55] K. Djordjev, S. J. Choi, and P. D. Dapkus, *IEEE Phot. Technol. Lett.* 14**:**828, 2002.

[56] A. Imamoglu, D. D. Awschalom, G. Burkard, D. P. DiVincenzo, D. Loss, M. Sherwin, and A. Small, *Phys. Rev. Lett.*, 83:4204, 1999.

[57] D. P. Cubian, M. Haddad, R. Andre, R. Frey, G. Roosen, J. L. A. Diego, and C. Flytzani, *Phys. Rev. B*, 67: 45308, 2003.

[58] F. Meier and D. D. Awschalom, *Phys. Rev. B,* 70:205329, 2004.

[59] W. H. Wang, S. Ghosh, F. M. Mendoza, X. Li, D. D. Awschalom, and N.Samarth, *Phys. Rev. B,* 71:155306, 2005.

[60] S. L. McCall, A. F. J. Levi, R. E. Slusher, S. J. Pearton, and R. A. Logan, *Appl. Phys. Lett. ,* 60:289, 1992.

[61] B. Gayral, J.-M. Gerard, B. Sermage, A. Lemaitre, and C. Dupuis, *Appl. Phys. Lett.,* 78:2828, 2001.

[62] E. Peter, P. Senellart, D. Martrou, A. Lemaitre, J. Hours, J. M. Gerard, and J. Bloch, *Phys. Rev. Lett.*, 95:067401, 2005.

[63] A. Imamoglu, D. D. Awschalom, G. Burkard, D. P. DiVincenzo, D. Loss, M. Sherwin, and A. Small, *Phys. Rev. Lett.* 83:4204, 1999.

[64] A. Imamoğlu, S. Falt, J. Dreiser, G. Fernandez, M. Atature, K. Hennessy, A. Badolato, and D. Gerace, *J. Appl. Phys.* 101:081602, 2007.

[65] S. Ishii, A. Nakagawa, T. Baba, *IEEE J. Sel. Topics Quantum Electron.*,12:1,2006.

[66] S. Ishii, T. Baba, *Appl. Phys. Lett.*, 87:181102, 2005.

[67] S. M. K. Thiyagarajan, *Doctoral dissertation*, USC, 2002.

[68] S. K. Kim, S. H. Kim, G. H. Kim, H. G. Park, D. J. Shin, and Y. H. Lee, *Appl. Phys. Lett.*, 84:861, 2004.

[69] A. Nakagawa, S. Ishii, and T. Baba, *Appl. Phys. Lett.,* 86:041112, 2005.

[70] M. Bayer, T. Gutbrod, J. P. Reithmaier, A. Forchel, T. L. Reinecke, P. A.Knipp, A. A. Dremin, and V. D. Kulakovskii, *Phys. Rev. Lett.* ,81:2582, 1998.

[71] T. Mukaiyama, K. Takeda, H. Miyazaki, Y. Jimba, and M. Kuwata-Gonokami, *Phys. Rev. Lett.*, 82:4623, 1999.

[72] X. Li, R. C. Myers, F. M. Mendoza, D. D. Awschalom, and N. Samarth, *IEEE J. Quantum Electron.*, 45:922, 2009.

[73] B. M. Möller, U. Woggon, M. V. Artemyev, and R. Wannemacher, *Phys. Rev. B* 70:115323, 2004.

[74] M. Bayer, T. Gutbrod, J. P. Reithemaier, and A. Forchel, *Phys. Rev. Lett.*, 81:2582, 1998.

[75] M. Bayer, T. Gutbrod, J. P. Reithemaier, and A. Forchel, *Phys. Rev. Lett.*, 81:2582, 1998.

[76] L. Goldstein, F. Glas, J. Y. Marzin, M. N. Charasse, and G. Le Roux , *Appl. Phys. Lett.*, 47:1099, 1985.

[77] G. J. Lasher, *Solid-State Electron.*, 7:707, 1964.

[78] C. Harder, K. Y. Lau, and A. Yariv, *Appl. Phys. Lett.*, 40:124, 1982.

[79] J. K. Carney and C. G. Fonstad, *Appl. Phys. Lett.*, 38:303, 1981.

[80] H. Kawaguchi, *Electron. Lett.*, 17:741, 1981.

[81] Y. Hori, H. Sato, H. Serizawa, and T. Kajiwara, *J. Appl. Phys.* 60:534, 1986.

[82] W. A. Stallard and D. J. Bradley, *ibid*, 42:858, 1983.

[83] M. Hercher, *Applied Optics,* 6:5, 1967.

[84] C. Fu, A. Grimes, M. Long, C. G.L. Ferri, B. D. Rich, S. N. Ghosh, Luke P. Lee, *Advanced Materials,* 21, 2009.

[85] G. K. Mor, J. Basham, M. Paulose, S. Kim, O. K. Varghese, A. Vaish, S. Yoriya and C. A. Grimes, *Nano Lett.*,10:2387, 2010.

[86] N. S. Lewis, Science 315:798, 2007.

[87] Gratzel, Nature 414:338, 2001.

[88] W. U. Huynh, J. J. Dittmer & A. P. Alivisatos, *Science*, 295:2425, 2002.

[89] M. Law, L. E. Greene, J. C. Johnson, R. Saykally & P. Yang, *Nature Mater.*, 4:455, 2005.

[90] J. B. Baxter and E. S. Aydil, *Appl. Phys.Lett.* ,86, 2005.

[100] A. Luque, A. Marti and A. J. Nozik, *MRS Bull.*,32:236, 2007.

[101] B. M. Kayes, H. A. Atwater, and N. S. Lewis, *J. Appl. Phys.*, 97:114302, 2005.

[102] Y. Zhang, L. W. Wang & Mascarenhas, *Nano Lett.*, 7:1264, 2007.

[103] H. Dai, E. W. Wang, Y. Z. Lu, S. Fan, C. M. Lieber, *Nature*, 375:769, 1995.

[104] J. R. Heath, P. J. Kuekes, G. Snyder, R. S. Williams, *Science,* 280:1717, 1998.

[105] M. A. Green, K. Emery, D. L. King, Y. Hishikawa, W. Warta *Prog. Photo*V*olt: Res. Appl., 15*:35, 2005.

[106] K. Ramanathan, M. A. Contreras, C. L. Perkins, S. Asher, F. S. Hasoon, J. Keane, D. Young, M. Romero, W. Metzger, R. Noufi, J. Ward, A. Duda, *Prog. Photo* V*olt: Res., 11*:225, 2003.

[107] E. J. Menke, M. A. Thompson, C. Xiang, L.C.Yang, R.M. Penner, *Nature Materials*, 5:914, 2006.

[108] S. Phok, S. Rajaputra and V. P Singh, *Nanotechnology,* 18**,** 2007.

[109] J. E. Hujdic, D. K. Taggart, S. C. Kung, and E. J. Menke, *Journal of Physical Chemistry Letters*,1:1055, 2010.

[110] D. A. Boyd, L. Greengard, M. Brongersma, M. Y. El-Naggar, D. G. Goodwin, *Nano Lett.,* 6:2592, 2006.

[111] K. W. Kho, Z. X. Shen, Z. Lei, F. Watt, K. C. Soo, M. Olivo, *Anal Chem.,*79:8870, 2007.

[112] C. X. Xiang, S. C. Kung, D. K. Taggart, F. Yang, M. A. Thompson, A. G. Guell, Y. A. Yang, and R. M. Penner, *ACS Nano*, 2:1939, 2008.

[113] L. Y. Cao, P. Y. Fan, A. P. Vasudev, J. S. White, Z. F. Yu, W. S. Cai, J. A. Schuller, S. H. Fan, M. L. Brongersma, *Nano Lett.*, 10:439, 2010.

[114] L. Y. Cao, J. S. White, J. S. Park, J. A. Schuller, B. M. Clemens,M. L. Brongersma, *Nat. Mater.,* 8:643, 2009.

[115] J. Tang, Z. Huo, S. Brittman, H. Gao, and P. Yang, *Nature Nanotechnology,* 6:568, 2011.

[116] T. Peng, H. Yang, K. Dai, X. Pu, K. Hirao, *Chem. Phys. Lett.*, 379:432, 2003.

[117] D. Routkevitch, T. Bigioni, M. Moskovits, J.M. Xu, J. Phys. Chem. 100:14037, 1996.

[118] K.V. Anikin, N.N. Melnik, A.V. Simakin, G.A. Shafeev, V.V. Voronov, A.G. Vitukhnovsky, *Chem. Phys. Lett.* 366 :357, 2002.

[119] C. J. Barrelet, Y. Wu, D. C. Bell, C. M. Lieber, *J. Am. Chem. Soc.* 125:11498, 2003.

[120] Y. J. Xiong, Y. Xie, J. Yang, R. Zhang, C.Z. Wu, G.A. Du, *J. Mater. Chem.* 12 :3712, 2002.

[121] D. Xu, Z. Liu, J. Liang, Y.T. Qian, *J. Phys. Chem. B*, 109:14344, 2005.

[122] D. Hariskos, S. Spiering, M. Powalla, *Thin Solid Films*, 480:99, 2005.

[123] S. N. Ghosh, J. Hujdic and E. Menke, *Journal of Physical Chemistry C,*115:17670, 2011.

[124] S. Brovelli,R. D. Schaller, S. A. Crooker, F. García-Santamaría,Y. Chen, R. Viswanatha, J. A. Hollingsworth, H. Htoon, and V. I. Klimov, *Nat Commun.* 2: 280, 2011.